machines

MDPI

Article

Hopf Bifurcation Characteristics of a Magnetic Liquid Double-Suspension Bearing Rotor System

Xinwei Wang [1,2], Xv Zhang [1,2], Hanwen Zhang [1,2] and Jianhua Zhao [1,2,*]

[1] School of Mechanical Engineering, Yanshan University, Qinhuangdao 066004, China
[2] Hebei Provincial Key Laboratory of Heavy Machinery Fluid Power Transmission and Control, Yanshan University, Qinhuangdao 066004, China
* Correspondence: zhaojianhua@ysu.edu.cn

Abstract

To reveal the nonlinear instability mechanism by which the three-degree-of-freedom rotor system of a magnetic-liquid double suspension bearing transforms from stable suspension to periodic vibration, a nonlinear dynamic model considering electromagnetic suspension force, hydrostatic supporting force, rotor unbalance force, and liquid film resistance is established. The equilibrium point of the system is linearized, and the Hopf bifurcation boundary is determined using the Routh–Hurwitz criterion. Numerical simulations are then carried out to investigate the effects of the initial current i_0, supply flow rate q_0, and different initial disturbances on the displacement time histories, phase trajectories, and spatial phase trajectories of the rotor. The results show that, under the given system parameters, the Hopf bifurcation boundary is 0.61 A for the initial current and 9.62×10^{-5} m^3/s for the supply flow rate. Current variation mainly affects electromagnetic stiffness and nonlinear electromagnetic force, whereas flow rate variation primarily changes the hydrostatic load capacity and oil film damping characteristics. Under different initial disturbances, the system may exhibit amplitude attenuation, recovery to stable suspension, or finite amplitude periodic vibration. Experimental results show good agreement with numerical simulations in terms of frequency spectra, displacement time histories, and phase trajectories, thereby verifying the effectiveness of the proposed three-degree-of-freedom dynamic model and Hopf bifurcation analysis method. The results can provide theoretical guidance for parameter matching, stability evaluation, and self-excited vibration suppression of magnetic-liquid double suspension bearings.

Keywords: magnetic liquid double-suspension bearing; three-degree-of-freedom rotor system; Hopf bifurcation; Routh–Hurwitz criterion; nonlinear stability

Check for updates

Academic Editor: Dimitrios Giagopoulos

Received: 11 May 2026
Revised: 7 June 2026
Accepted: 12 June 2026
Published: 17 June 2026

Copyright: © 2026 by the authors. Licensee MDPI, Basel, Switzerland. This article is an open access article distributed under the terms and conditions of the Creative Commons Attribution (CC BY) license.

1. Introduction

With the development of high-performance rotating machinery toward medium-to-high rotational speeds, heavy loading, high precision, and high stability, bearing systems are required to provide high load-carrying capacity, supporting stiffness, damping performance, and dynamic regulation capability. Active magnetic bearings offer several advantages, including non-contact support, active control, and vibration suppression, and have therefore been widely used in flexible rotor dynamic control and stability studies of rotating machinery. Hydrostatic bearings, in contrast, are characterized by high load-carrying capacity, high stiffness, and high operating accuracy, which make them particularly valuable for heavy-load and high-precision equipment [1–3]. However, a single supporting

configuration often cannot simultaneously satisfy the requirements for active regulation, high load-carrying capacity, and high damping. To improve the supporting performance of rotor systems under medium-speed, heavy-load, and frequent start–stop operating conditions, the magnetic liquid double-suspension bearing integrates electromagnetic suspension support with hydrostatic support. In this configuration, electromagnetic support provides active regulation, whereas the hydrostatic oil film enhances the load-carrying capacity and supporting stiffness. This combined supporting mechanism gives the bearing considerable potential for high-stability rotating machinery [4,5].

Although the hybrid supporting structure can improve the load capacity and regulation performance of the rotor system, the coupled action of electromagnetic support and hydrostatic support also leads to more complex dynamic behavior. In active magnetic bearing rotor systems, the electromagnetic force usually exhibits a nonlinear dependence on the coil current and air gap. Variations in operating parameters may therefore alter the static equilibrium position, periodic response, and bifurcation behavior of the system. In liquid bearing or oil film-supported systems, the oil film force, stiffness, and damping may also vary with rotational speed, load, and liquid film state, giving rise to pronounced nonlinear characteristics. Previous studies on rotating machinery have shown that changes in supporting parameters and operating conditions may induce nonlinear phenomena such as Hopf bifurcation, multivalued responses, limit cycle oscillations, and oil film instability [6–8]. For a magnetic liquid double-suspension bearing, the electromagnetic suspension force and hydrostatic supporting force act on the rotor simultaneously and, together with the rotor unbalance force and liquid film resistance, determine the stability of the system. When the current, flow rate, or external disturbance, is not properly matched, the rotor may lose its stable suspension state and evolve into finite-amplitude periodic vibration. Hopf bifurcation describes the critical process in which an equilibrium point loses stability, and a periodic response emerges. It is therefore well-suited for analyzing the dynamic mechanism by which a magnetic liquid double-suspension bearing rotor system transitions from stable suspension to self-excited vibration. Hopf bifurcation and vibration control in magnetic bearing rotor systems have also been used to explain changes in the stability of periodic motion under nonlinear magnetic forces [9].

In recent years, nonlinear dynamics and bifurcation theory have been widely applied to stability analyses of magnetic bearings, liquid bearings, and rotor bearing systems. For active magnetic bearing systems, Ji and Hansen [10] investigated the influence of time delay in PD feedback control on the dynamic stability of a magnetic bearing rotor. They established a two-DOF nonlinear differential equation model incorporating time-delay coupling terms and showed that, when the time delay exceeds a critical value, the rotor equilibrium position becomes unstable and undergoes Hopf bifurcation, giving rise to different forms of periodic motion. Zhang et al. [11] further examined the stability and Hopf bifurcation of a magnetic suspension system with delayed position and velocity feedback. The stability conditions were derived using the characteristic root method, and the bifurcation direction, stability of periodic solutions, and period estimation were analyzed based on the center manifold theorem and the Poincaré normal form. These studies indicate that feedback control, time delay, and electromagnetic force nonlinearity in electromagnetic supporting systems substantially influence local stability and are important factors that may trigger Hopf bifurcation and periodic vibration. In addition to time-delay effects and feedback control, recent studies have paid increasing attention to nonlinear magnetic force modeling and parameter-dependent stability in active magnetic bearing rotor systems. Wang et al. [12] investigated nonlinear vibration control of a magnetic bearing system, considering positive and negative stiffness, showing that feedback gains and stiffness characteristics may induce complex nonlinear responses. Yao and Inayat-Hussain [13] analyzed the nonlinear

dynamics of a geared rotor system supported by active magnetic bearings and indicated that the nonlinear relationship among magnetic force, air gap, and coil current, together with the coupling between orthogonal magnetic actuators, can significantly affect rotor dynamic responses. Kandil [14] further developed a generalized pole pair model for active magnetic bearings, in which rotor oscillations governed by nonlinear differential equations were analyzed using harmonic balance and Floquet theory. These studies indicate that electromagnetic nonlinearity, control parameters, air gap variation, and support coupling are important factors affecting the stability and bifurcation behavior of magnetically supported rotor systems.

For liquid bearings and oil film-supported rotor systems, existing studies have mainly focused on how oil film force, supporting stiffness, damping, and rotational speed affect nonlinear system responses. Shen et al. [15] developed a fluid film force model considering Reynolds boundary conditions and applied it to the nonlinear dynamic analysis of a rigid rotor supported by elliptical bearings. Their results showed that a balanced rotor undergoes supercritical Hopf bifurcation as the rotational speed increases, whereas an unbalanced rotor may exhibit complex responses, including synchronous motion, subharmonic motion, quasiperiodic motion, and chaos. Wang and Khonsari [16] proposed a stability envelope prediction method for rotor bearing systems based on Hopf bifurcation theory. The method was used to determine the instability boundary of the system, and its predictions were compared with previously reported results obtained by trial-and-error methods. Recently, Lee et al. [6] performed nonlinear steady state and stability analyses of a rotor system supported by hydrodynamic bearings using the harmonic balance method. They pointed out that linearization methods are insufficient for capturing nonlinear response features such as superharmonic components and resonance. These studies indicate that the stability of liquid film-supported systems is governed not only by their static load-carrying capacity but also by nonlinear oil film forces, damping characteristics, and the evolution of post-bifurcation responses.

With the development of hybrid supporting technologies, the dynamic behavior of hybrid-supported rotor systems has also attracted increasing attention. Zhang et al. [17] investigated the nonlinear dynamic characteristics of a rotor supported by hybrid foil and magnetic bearings and validated the rotor dynamic model through run-down tests. Their results indicated that the operating mode and load-sharing ratio have a pronounced influence on rotor dynamic performance, and that an appropriate load distribution can improve system stability. For magnetic liquid double-suspension bearings, Zhao et al. [4] investigated the influence of controller parameters on the static bifurcation behavior. They established a mathematical model of the magnetic liquid double-suspension bearing and analyzed how control parameters affect the properties of singular points, phase trajectories, and basins of attraction. Their study showed that the coupled action of electromagnetic support and hydrostatic support increases the likelihood of bifurcation and affects operational stability. Zhang et al. [18] further examined the chaotic dynamic behavior of a magnetic liquid double-suspension bearing under rub-impact faults. They formulated the rotor dynamic equations for the rub-impact condition and analyzed the effects of structural and operating parameters on the bifurcation behavior of the system using bifurcation diagrams, phase portraits, and experimental results.

In summary, previous studies have clarified the influence of supporting parameters and nonlinear forces on system stability from the perspectives of magnetic bearing systems, liquid bearing systems, and fault dynamics of magnetic liquid double-suspension bearings. These studies provide an important basis for bifurcation analysis of hybrid-supported rotor systems. Nevertheless, several issues remain unresolved. Existing studies on magnetic liquid double-suspension bearings have mainly focused on single-DOF supporting models,

static bifurcation, the influence of control parameters, or complex responses under rub-impact faults. In contrast, the Hopf bifurcation boundary of a three-DOF rotor system under normal suspension conditions has not been sufficiently investigated. Moreover, under the combined action of electromagnetic suspension force, hydrostatic supporting force, rotor unbalance force, and liquid film resistance, coupled dynamic characteristics exist among the x and y radial directions and the rotational degree of freedom. A single-DOF model is therefore insufficient to fully describe the post-bifurcation evolution of time histories, phase trajectories, and limit cycles. It is therefore necessary to establish a three-DOF dynamic model of a magnetic liquid double-suspension bearing rotor system and further analyze its Hopf bifurcation boundary and post-bifurcation dynamic responses.

To address these issues, this study focuses on a three-degree-of-freedom rotor system supported by a magnetic liquid double-suspension bearing. The main contributions of this study are summarized as follows. First, a nonlinear dynamic model of the three-degree-of-freedom rotor system is established by incorporating the electromagnetic suspension force, hydrostatic supporting force, rotor unbalance force, and liquid film resistance, thereby providing the modeling basis for subsequent stability analysis. Second, the equilibrium point of the system is linearized to construct the Jacobian matrix, and the Hopf bifurcation boundary is determined based on the Routh–Hurwitz criterion, thereby providing a theoretical basis for evaluating the local stability of the rotor system. Third, the current i_0 and supply flow rate q_0 are selected as the main operating parameters, and their individual and coupled effects on the Hopf bifurcation characteristics are analyzed through time histories, phase trajectories, and spatial phase trajectories under different parameter combinations and initial disturbance conditions. This analysis clarifies the dynamic mechanism by which the rotor system transitions from stable suspension to periodic vibration. Finally, rotor displacement signals are acquired using a magnetic liquid double-suspension bearing test system, and the experimental results are compared with the numerical simulations to validate the proposed model and Hopf bifurcation analysis method. This study provides a theoretical basis for operating parameter matching, stability evaluation, and self-excited vibration suppression in magnetic liquid double-suspension bearings.

2. Three-Degree-of-Freedom Dynamic Model and Hopf Bifurcation Analysis Method

A magnetic liquid double-suspension bearing consists of electromagnetic suspension support and hydrostatic support. The stable suspension state of the rotor is governed by the combined effects of electromagnetic force, hydrostatic supporting force, rotor unbalance force, and liquid film resistance. The electromagnetic suspension force is nonlinearly dependent on the coil current and working air gap, while the hydrostatic supporting force is also nonlinearly dependent on the supply flow rate and the liquid film thickness. Therefore, variations in operating parameters, such as current and flow rate, may cause Hopf bifurcation near the equilibrium position of the rotor system, leading to self-excited vibration. To investigate the influence of electromagnetic and hydrostatic coupling parameters on rotor stability, a three-degree-of-freedom dynamic model of the magnetic liquid double-suspension bearing rotor system is established, and the Hopf bifurcation boundary is determined based on the Routh–Hurwitz criterion.

2.1. Three-Degree-of-Freedom Rotor Dynamic Model

For modeling convenience, the following assumptions are adopted: magnetic leakage in the electromagnetic coils is neglected; the liquid flow in the supporting chambers is assumed to be laminar; and the rotor undergoes small-amplitude motion near the equilibrium position, so that variations in the supporting clearance can be approximated

by the rotor displacement [19]. Under these assumptions, the electromagnetic suspension forces and hydrostatic supporting forces acting on the rotor in the x- and y-radial directions can be obtained from electromagnetic suspension theory and hydrostatic bearing theory.

The electromagnetic supporting force of the magnetic liquid double-suspension bearing is produced by the attraction between the stator magnetic poles and the rotor. Its magnitude depends mainly on the coil current and the working air gap. Under the centered equilibrium condition, the forces generated by two opposite magnetic poles are balanced. Once the rotor is displaced from the equilibrium position, the opposite air gaps vary in opposite directions. The control current is then differentially added to and subtracted from the bias current, producing an unbalanced electromagnetic force that acts as the restoring force of the rotor.

In the equilibrium state, the clearances between the bearing rotor and the upper and lower supporting units are identical. The initial current in the electromagnetic coils wound on the stator is denoted as i_0, and the initial control current is denoted as i_c. According to Maxwell's electromagnetic equations, the electromagnetic forces F_{d1} and F_{d2} acting on the rotor of the magnetic liquid double-suspension bearing when it is located at the center position can be expressed as follows:

$$\begin{cases} F_{d1} = 2k\frac{(i_0 - i_c)^2}{\delta_0^2}\cos\theta \\ F_{d2} = 2k\frac{(i_0 + i_c)^2}{\delta_0^2}\cos\theta \end{cases} \quad (1)$$

where

N — number of turns of the electromagnetic coil, dimensionless
δ_0 — air gap (m), $\delta_0 = h_0 + 2l$
l — coating thickness (m)
k — electromagnetic constant (H·m), $k = \mu_0 N^2 S/4$.
S — iron core area (m^2)
μ_0 — magnetic permeability (H/m), $\mu_0 = 4\pi \times 10^{-7}$

When the bearing rotor is subjected to an external disturbance, the equilibrium position shifts. As a result, the lower air gap h_2 decreases, whereas the upper air gap h_1 increases. If the rotor displacement is denoted as x, the air gaps can be expressed as follows:

$$\begin{cases} \delta_1 = \delta_0 + x\cos\theta \\ \delta_2 = \delta_0 - x\cos\theta \end{cases} \quad (2)$$

To restore the bearing rotor to the equilibrium position, a PD control law is adopted: $i_{cy} = i_{y_0} + K_p x + K_d \dot{x}$, where i_{cy} is the control current, K_d is the derivative coefficient, and K_p is the proportional coefficient.

Substituting Equation (2) into Equation (1) gives the electromagnetic suspension forces F_{d1} and F_{d2} acting on the upper and lower sides of the bearing rotor as follows:

$$\begin{cases} F_{d1} = 2k\frac{(i_0 + i_c + K_p x + K_d x')^2}{(\delta_0 + x\cos\theta)^2}\cos\theta \\ F_{d2} = 2k\frac{(i_0 - i_c - K_p x - K_d x')^2}{(\delta_0 - x\cos\theta)^2}\cos\theta \end{cases} \quad (3)$$

The oil supply mode of the hydrostatic supporting system for the bearing rotor is based on a constant flow rate. The basic structure of the hydrostatic supporting chamber is shown in Figure 1.

As shown in Figure 1, in the equilibrium state, the liquid film thickness between the upper and lower supporting units and the bearing rotor is h_0. The inlet flow rate of the supporting chamber is equal to the outlet flow rate of the proportional valve. Therefore, the

load-carrying forces F_{y1} and F_{y2} of the hydrostatic supporting chamber can be expressed as follows:

$$F_{y1} = F_{y2} = q_0 R_0 A_e \cos\theta \tag{4}$$

where

q_0 — initial flow rate (m^3/s)
R_0 — initial hydraulic resistance ($N{\cdot}s/m^5$), $R_0 = \mu/\overline{B}h_0^3$
A_e — load-carrying area of the oil chamber (m^2)
θ — included angle between supporting chambers (deg)
μ — hydraulic oil viscosity ($Pa{\cdot}s$)
$\overline{B}$ — support coefficient, dimensionless

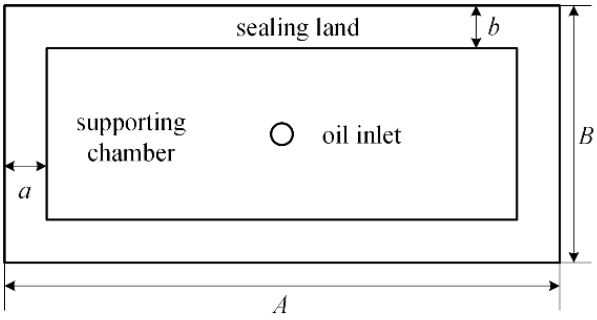


Figure 1. Basic structure of the hydrostatic supporting chamber.

The oil film thicknesses h_1 in the upper supporting chamber and h_2 in the lower supporting chamber vary with the actual operating conditions. Their mathematical expressions are given as follows:

$$\begin{cases} h_1 = h_0 + x\cos\theta \\ h_2 = h_0 - x\cos\theta \end{cases} \tag{5}$$

Similarly, the flow rates q_1 and q_2 in the upper and lower supporting chambers can be expressed as follows:

$$\begin{cases} q_1 = q_0 - A_b h_1' \\ q_2 = q_0 + A_b h_2' \end{cases} \tag{6}$$

where

A_b — squeeze area of the supporting chamber (m^2)
q_1 — flow rate in the upper supporting chamber (m^3/s)
q_2 — flow rate in the lower supporting chamber (m^3/s)

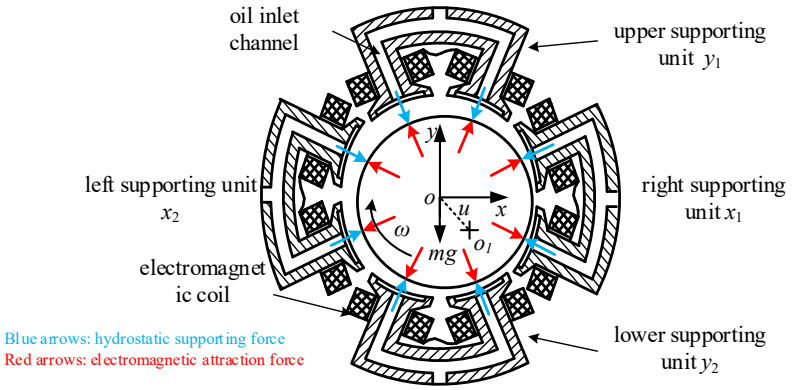
Substituting Equation (6) into Equation (4) yields the mathematical expressions for the hydrostatic supporting force F_{y1} in the upper supporting chamber and the hydrostatic supporting force F_{y2} in the lower supporting chamber under actual operating conditions:

$$\begin{cases} F_{y1} = q_1 R_1 A_e \cos\theta \\ F_{y2} = q_2 R_2 A_e \cos\theta \end{cases} \tag{7}$$

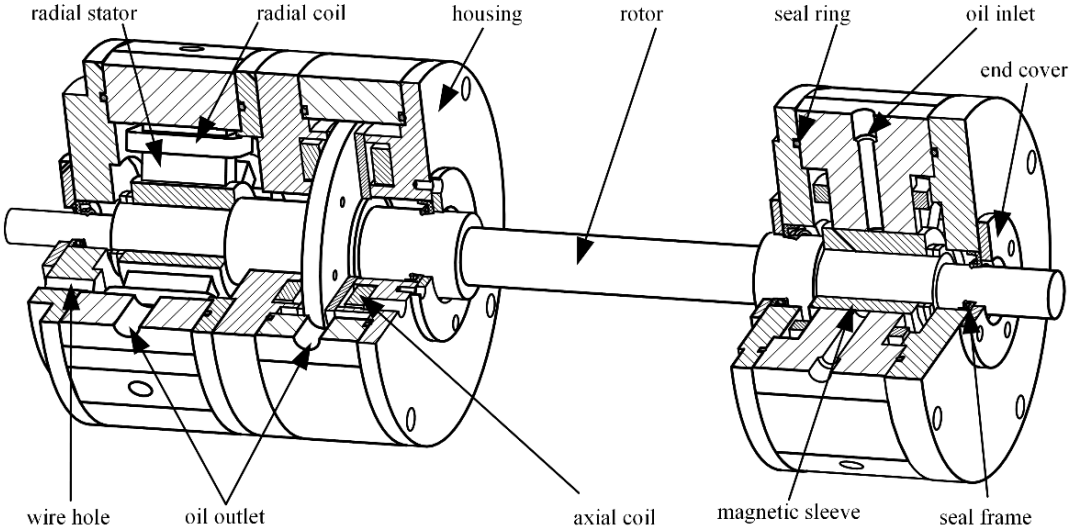
where

R_1 — hydraulic resistance of the upper supporting chamber ($N{\cdot}s/m^5$), $R_1 = \mu/\overline{B}h_1^3$
R_2 — hydraulic resistance of the lower supporting chamber ($N{\cdot}s/m^5$), $R_2 = \mu/\overline{B}h_2^3$

The mechanical model and three-dimensional structural schematic of the three-degree-of-freedom rotor supporting system are shown in Figure 2. Figure 2a shows the mechanical model, and Figure 2b presents the rotor with left- and right-hand support units.



(**a**) Mechanical model of the radial supporting system



(**b**) Three-dimensional schematic of the rotor with left- and right-hand supports

Figure 2. Mechanical model and three-dimensional structural schematic of the three-degree-of-freedom rotor supporting system.

The three-degree-of-freedom model is developed from the single-degree-of-freedom radial support model by accounting for the coupled radial and rotational motion of the rotor. Specifically, the translational motions in the x and y directions are governed by Newton's second law, and the rotational motion is governed by the angular momentum theorem. The electromagnetic supporting force, hydrostatic supporting force, rotor unbalance force, and gravity are included in the translational force balance, while the liquid film resistance produces the moment associated with the rotational degree of freedom. Combining the electromagnetic suspension force given in Equation (3) with the hydrostatic supporting force given in Equation (7), the dynamic equations of the three-degree-of-freedom magnetic liquid double-suspension bearing can be obtained as follows.

1. Electromagnetic Suspension Force

The three-degree-of-freedom bearing rotor system is still controlled using a PD control strategy. Based on the electromagnetic suspension force expression for the single-degree-of-freedom system, the electromagnetic suspension forces of the three-degree-of-freedom bearing rotor system can be formulated as follows:

$$\begin{cases} F_{dx} = F_{Mx,1} - F_{Mx,2} \\ F_{dy} = F_{My,1} - F_{My,2} \end{cases} \tag{8}$$

where

$$\begin{cases} F_{Mx,j} = 2k\cos\theta \sum\limits_{j=1}^{2} (-1)^{j+1} \left[\dfrac{i_0 + (-1)^j (i_c + k_p x + k_d x')}{(h_0 + (-1)^j x\cos\theta)} \right]^2 \\ F_{My,j} = 2k\cos\theta \sum\limits_{j=1}^{2} (-1)^{j+1} \left[\dfrac{i_0 + (-1)^j (i_c + k_p y + k_d y')}{(h_0 + (-1)^j y\cos\theta)} \right]^2 \end{cases} \tag{9}$$

2. Hydrostatic Supporting Force

Considering the actual operating conditions, the squeezing effect of the bearing rotor on the hydraulic oil film during rotation is incorporated. The hydrostatic supporting forces of the three-degree-of-freedom bearing rotor system can then be formulated as follows:

$$\begin{cases} F_{Lx} = F_{Lx,2} - F_{Lx,1} \\ F_{Ly} = F_{Ly,2} - F_{Ly,1} \end{cases} \tag{10}$$

where

$$\begin{cases} F_{Lx,j} = \dfrac{\mu(q_0 - A_b x')}{\overline{B}} \sum\limits_{j=1}^{2} (-1)^{j+1} \left[(h_0 + (-1)^j x\cos\theta)^3 \right] \\ F_{Ly,j} = \dfrac{\mu(q_0 - A_b y')}{\overline{B}} \sum\limits_{j=1}^{2} (-1)^{j+1} \left[(h_0 + (-1)^j y\cos\theta)^3 \right] \end{cases} \tag{11}$$

3. Rotor Unbalance Force

The bearing rotor is inevitably subjected to unbalance forces caused by manufacturing and assembly errors. By decomposing the rotor unbalance force along the x and y directions, the unbalance force components u_x and u_y can be expressed as follows:

$$\begin{cases} u_x = me\omega^2\cos(\omega t + \alpha) \\ u_y = me\omega^2\sin(\omega t + \alpha) \end{cases} \tag{12}$$

where

u_x — axial unbalance force (N)
u_y — radial unbalance force (N)
e — rotor eccentricity (μm)
α — initial phase angle of the mass-center offset (rad)
ω — rotor angular velocity (rad/s)

For subsequent analysis, the rotor unbalance is decomposed into eccentricity components along the x and y directions. The corresponding unbalance force components u_x and u_y can then be simplified as follows:

$$\begin{cases} u_x = me_x\omega^2\cos(\omega t) + me_y\omega^2\sin(\omega t) \\ u_y = -me_x\omega^2\sin(\omega t) + me_y\omega^2\cos(\omega t) \end{cases} \tag{13}$$

where

e_x, e_y — eccentricity components in the x and y directions (m)

4. Three-Degree-of-Freedom Dynamic Equations

According to Figure 2, the liquid film resistance acting on the bearing rotor at different rotational speeds is denoted as F_t. The three-degree-of-freedom dynamic equations are then established as follows:

$$\begin{cases} F_{Lx} + F_{Mx} + u_x = mx'' \\ F_{Ly} + F_{My} + u_y + mg = my'' \\ J\theta'' = -F_t r \end{cases} \tag{14}$$

where

F_t — liquid film resistance (N)
r — shaft radius (m)
J — moment of inertia (kg·m^2)

The three-degree-of-freedom dynamic equations of the magnetic liquid double-suspension bearing system derived in Equation (14) are reduced to an autonomous system for analysis. In the local stability analysis near the equilibrium point, the synchronous unbalanced excitation of the rotor is treated as a steady excitation term under a prescribed operating condition. The analysis therefore focuses on the effects of variations in electromagnetic support and hydrostatic support parameters on the characteristic roots of the lateral vibration subsystem.

$$\begin{cases} x_1 = x_2 \\ x_2' = \frac{1}{m}(F_{Lx} + F_{Mx} + U_x) \\ x_3 = x_4 \\ x_4' = \frac{1}{m}(F_{Ly} + F_{My} + U_y + mg) \\ x_5 = x_6 \\ x_6' = -\frac{1}{J}(F_t r) \end{cases} \tag{15}$$

where

x_1, x_2, x_3 — displacement terms of the system
x_2', x_4', x_6' — velocity terms of the system
F_{Mx}, F_{My} — electromagnetic suspension forces in the x and y directions (N)
U_x, U_y — axial unbalance force and radial unbalance force (N)
r — rotor radius (m)
m — mass of the bearing rotor (kg)
J — moment of inertia of the rotor (kg·m^2)
F_t — liquid film resistance (N)

To improve the reproducibility of the theoretical analysis and numerical simulations, the main parameters used in this study are summarized in Table 1.

Table 1. Main parameters used in the theoretical analysis and numerical simulations.

Parameter	Value	Parameter	Value
Included angle between supporting chambers θ (°)	22.5	iron core area S (mm^2)	1080
Magnetic permeability μ_0 (H/m)	$4\pi \times 10^{-7}$	Current i_0 (A)	1.4
Number of turns of the electromagnetic coil N	50	Gravitational acceleration g (m/s^2)	9.8
Squeeze area of the supporting chamber A_b (mm^2)	56	Mass of the bearing rotor m (kg)	10
Hydraulic oil viscosity μ (m Pa·s)	41.36	Liquid film thickness h_0 (μm)	70
Support coefficient, dimensionless $\overline{B}$	0.6820	Load-carrying area of the oil chamber A_e (mm^2)	416
Initial flow rate q_0 (m^3/s)	5×10^{-5}	Air gap δ_0 (mm)	0.5

2.2. Hopf Bifurcation Criterion

Several methods can be used for stability analysis of nonlinear rotor-bearing systems, such as eigenvalue analysis, Lyapunov stability theory, Nyquist criterion, Floquet theory, and numerical continuation methods. These methods are suitable for different stability problems. For the present study, the Hopf bifurcation boundary is determined from the local stability of the equilibrium point after linearization. Therefore, the Routh–Hurwitz

criterion is adopted because it can provide algebraic stability conditions directly from the characteristic polynomial of the linearized system.

In this study, the bifurcation parameters are selected according to the supporting mechanism of the magnetic liquid double-suspension bearing. The current i_0 directly affects the electromagnetic suspension force and its equivalent stiffness, whereas the supply flow rate q_0 directly influences the hydrostatic supporting force, oil film load-carrying capacity, and damping characteristics. Therefore, i_0 and q_0 represent the dominant regulation effects of the electromagnetic support subsystem and the hydrostatic support subsystem, respectively. By analyzing the Hopf bifurcation behavior induced by their individual and coupled effects, the influence of electromagnetic and hydrostatic coupling parameters on rotor stability can be clarified.

The full three-degree-of-freedom model includes the radial translational motions in the x and y directions and the rotational motion of the rotor. In this study, the Hopf bifurcation is mainly related to the local stability loss of the radial suspension state. Therefore, the lateral vibration subsystem is extracted from the full model to establish the Hopf bifurcation criterion. The rotational degree of freedom is still retained in the complete model and affects the dynamic response through the liquid film resistance and coupling terms.

The equilibrium point $O = (0, 0, 0, 0, 0, 0)$ is defined with respect to the static suspension equilibrium position of the rotor. At this position, the electromagnetic supporting force, hydrostatic supporting force, gravity, and steady excitation terms are balanced. Therefore, the origin represents the stable suspension state of the rotor in the relative displacement coordinate system.

The Jacobian matrix of the bearing rotor system at the equilibrium point $O = (x_1, x_2, x_3, x_4, x_5, x_6) = (0, 0, 0, 0, 0, 0)$ is obtained as follows:

$$Df_x(x_0, u) = \begin{bmatrix} \frac{\partial \dot{x}_1}{\partial x_1} & \frac{\partial \dot{x}_1}{\partial x_2} & \cdots & \frac{\partial \dot{x}_1}{\partial x_6} \\ \frac{\partial \dot{x}_2}{\partial x_1} & \frac{\partial \dot{x}_2}{\partial x_2} & \cdots & \frac{\partial \dot{x}_2}{\partial x_6} \\ \vdots & \vdots & \ddots & \vdots \\ \frac{\partial \dot{x}_6}{\partial x_1} & \frac{\partial \dot{x}_6}{\partial x_2} & \cdots & \frac{\partial \dot{x}_6}{\partial x_6} \end{bmatrix} = \begin{bmatrix} 0 & 1 & 0 & 0 & 0 & 0 \\ a_1 & a_2 & 0 & 0 & 0 & 0 \\ 0 & 0 & 0 & 1 & 0 & 0 \\ 0 & 0 & a_3 & a_4 & 0 & 0 \\ 0 & 0 & 0 & 0 & 1 & 0 \\ 0 & 0 & 0 & 0 & 0 & a_5 \end{bmatrix} \tag{16}$$

where

$$a_1 = \frac{4ck}{m}\left(\frac{2c{i_0}^2}{(h_0+2l)^3} - \frac{300i_0K_p}{(h_0+2l)^2}\right) - \frac{6A_ec^2q_0u}{(B_1(h_0+2l)^4)};$$

$$c = \frac{8i_0kk_d\cos\theta}{{\delta_0}^2} + \frac{4A_b\mu q_0\cos\theta}{\overline{B}h_0^3}$$

$$a_2 = -\frac{1200ci_0kK_d}{m(h_0+2l)^2} - \frac{2A_bA_ec^2u}{B_1(h_0+2l)^3};$$

$$a_3 = \frac{2ck}{m}\left(\frac{2c{i_0}^2}{(h_0+2l+cg)^3} - \frac{300i_0K_p}{(h_0+2l+cg)^2}\right) + 2ck\left(\frac{2c{i_0}^2}{(h_0+2l-cg)^3} - \frac{300i_0K_p}{(h_0+2l-cg)^2}\right); \\ -\frac{3A_ec^2q_0u}{(B_1(h_0+2l+cg)^4)^2} - \frac{3A_ec^2q_0u}{B_1(h_0+2l-cg)^4}$$

$$a_4 = -\frac{1}{m}\left(\frac{600ci_0kK_d}{(h_0+2l+cg)^2} + \frac{600ci_0kK_d}{(h_0+2l-cg)^2} + \frac{A_bA_ec^2u}{B_1(h_0+2l+cg)^3} + \frac{A_bA_ec^2u}{B_1(h_0+2l-cg)^3}\right);$$

$$a_5 = \frac{1}{J}(F_tr).$$

Because this study focuses on the lateral vibration stability in the x and y radial directions, the rotational degree of freedom mainly affects the damping characteristics of

the system through the liquid film resistance term. Therefore, the Hopf bifurcation criterion is established for the four-dimensional lateral subsystem. The characteristic polynomial of the *Jacobian* matrix at the rotor equilibrium point is obtained as follows:

$$\lambda^4 + R_1\lambda^3 + R_2\lambda^2 + R_3\lambda + R_4 = 0 \tag{17}$$

where

λ — independent variable of the characteristic polynomial
R_1 — coefficient, $R_1 = a_2 + a_4$
R_2 — coefficient, $R_2 = a_1 + a_3 + a_2a_4$
R_3 — coefficient, $R_3 = a_1\ a_4 + a_2a_3$
R_4 — coefficient, $R_4 = a_1a_3$

The Routh–Hurwitz criterion for Hopf bifurcation of the system is given as follows:

$$\begin{cases} R_1 > 0 \\ R_2 > 0 \\ R_1R_2 - R_3 > 0 \\ {R_1}^3 - 4R_1R_2 + 4R_3 \geq 0 \\ R_4 = \frac{R_1R_2R_3 - {R_3}^2}{{R_1}^2} \end{cases} \tag{18}$$

For the characteristic polynomial of the lateral vibration subsystem, the Routh–Hurwitz criterion is used to determine whether all characteristic roots remain in the left half of the complex plane. When the system parameters vary and the critical equality condition is satisfied, a pair of conjugate roots crosses the imaginary axis while the remaining roots remain stable. This condition is taken as the Hopf bifurcation boundary in this study.

When the characteristic equation has a pair of purely imaginary roots, Hopf bifurcation occurs near the equilibrium point of the system. By varying i_0 and q_0, the Hopf bifurcation boundaries can be obtained for three cases: current as the only varying parameter, flow rate as the only varying parameter, and current and flow rate varied simultaneously.

After the theoretical bifurcation boundaries are obtained, numerical integration is further employed to analyze the post-bifurcation dynamic responses. Small and large initial disturbances are prescribed separately, and the time histories, phase trajectories, and spatial phase trajectories of the rotor are calculated under different parameter combinations. The bifurcation response characteristics of the system are then identified by examining whether the response converges, whether a limit cycle is formed, and how the vibration amplitude evolves.

3. Hopf Bifurcation Characteristics Under the Effects of Current and Flow Rate

Based on the three-degree-of-freedom dynamic model of the magnetic liquid double-suspension bearing rotor system, the current i_0 and supply flow rate q_0 are selected as the main bifurcation parameters. The Hopf bifurcation behavior is analyzed under variations in the electromagnetic support parameters, the hydrostatic support parameters, and their coupled effects. The current i_0 mainly affects the electromagnetic suspension force and its equivalent stiffness, whereas the supply flow rate q_0 primarily influences the hydrostatic supporting force, liquid film load-carrying capacity, and oil film damping characteristics. Therefore, these two parameters characterize the regulatory effects of the electromagnetic and hydrostatic support subsystems on rotor stability. In the preceding section, the Hopf bifurcation analysis method was established based on the three-degree-of-freedom model, the *Jacobian* matrix, and the Routh–Hurwitz criterion. The numerical calculations and simulations were performed using MATLAB R2018a (MathWorks, Natick, MA, USA).

3.1. Effect of Current i_0 on Hopf Bifurcation Behavior

The current i_0 is a key operating parameter in the electromagnetic support system. According to the expression of the electromagnetic suspension force, the electromagnetic force exhibits a pronounced nonlinear dependence on the coil current and working air gap. When the current varies, the gradient of the electromagnetic suspension force changes accordingly, thereby affecting the equivalent stiffness and local stability of the rotor system. Taking the current i_0 as the single bifurcation parameter while keeping the other structural and operating parameters unchanged, the characteristic equation is evaluated together with the Routh–Hurwitz criterion. The Hopf bifurcation boundary of the three-degree-of-freedom rotor system is then obtained as $i_0 = 0.61$ A.

When the current crosses this critical value, the real part of the characteristic roots passes through zero, and the stability of the equilibrium point changes. Consequently, the rotor system transitions from stable suspension to periodic vibration.

Under a small initial disturbance, a numerical simulation is performed at $i_0 = 1$ A. The time-history response in Figure 3 shows that the rotor remains in a stable suspension state in the x direction for approximately the first 2.3 s. The vibration amplitude then increases gradually and eventually develops into a stable periodic response with an amplitude range of approximately $(-1.3 \times 10^{-7}, 1.3 \times 10^{-7})$ m. In the y direction, the rotor maintains stable suspension for approximately the first 2.0 s, after which small-amplitude vibration appears. During 2.3–2.5 s, the vibration amplitude increases rapidly and finally evolves into a periodic response with an amplitude range of approximately $(-1.4 \times 10^{-7}, 1.4 \times 10^{-7})$ m.

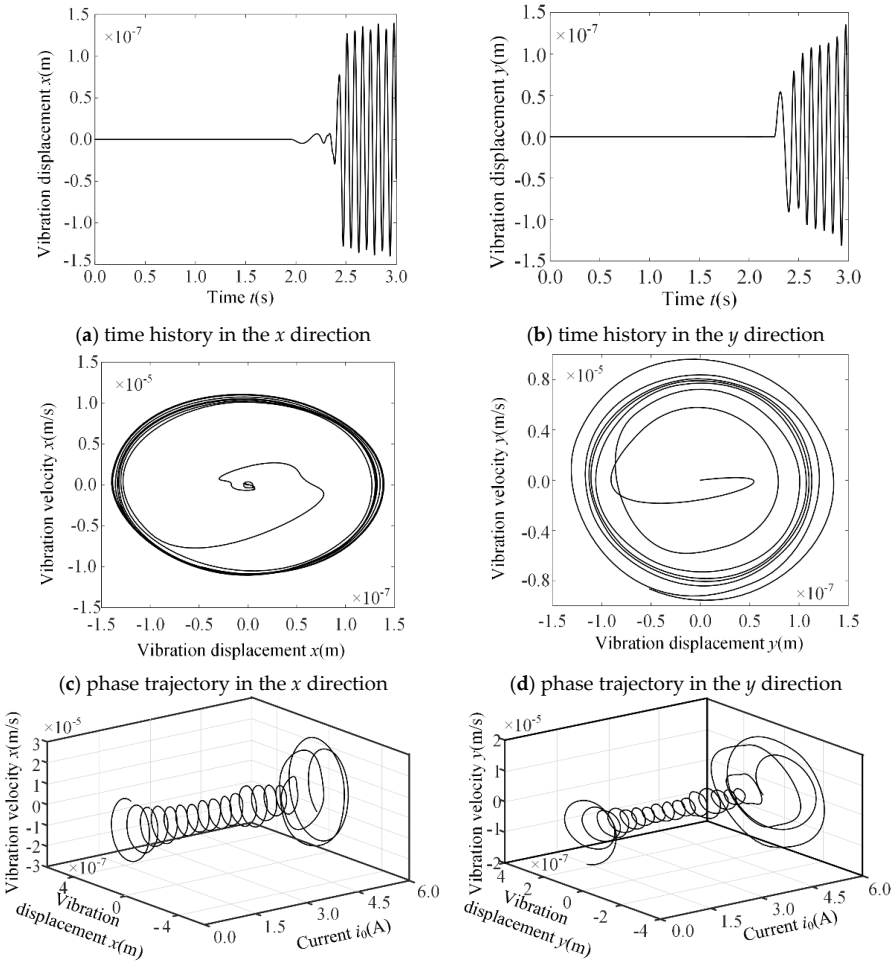


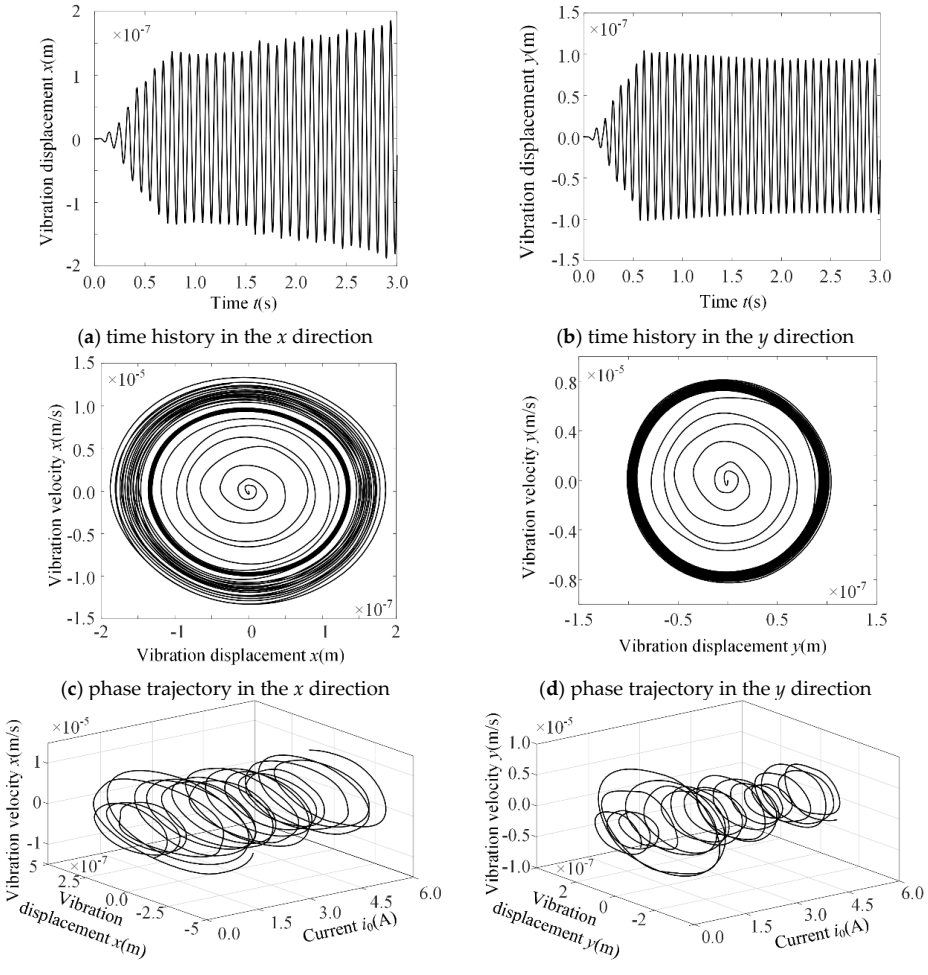
Figure 3. Bifurcation diagram of current i_0 under a small initial disturbance.

The phase trajectory gradually expands outward from the vicinity of the equilibrium point and eventually forms a closed orbit, indicating the emergence of limit cycle motion under the effect of current variation. This behavior demonstrates that, once the current exceeds the Hopf bifurcation boundary, the rotor system loses its stable suspension state and transitions to periodic vibration.

The spatial phase trajectories indicate that, as the current i_0 increases from the bifurcation boundary of 0.61 A to 6 A, the system exhibits instability-induced bifurcation characteristics in both the x and y directions. In the range of $i_0 \in (4.5, 6)$ A, the maximum vibration amplitude in the x direction is approximately $(-2 \times 10^{-7}, 2 \times 10^{-7})$ m, while that in the y direction is approximately $(-3 \times 10^{-7}, 3 \times 10^{-7})$ m.

This indicates that the influence of the electromagnetic support force on rotor stability becomes stronger as the current increases. However, once the current exceeds a reasonable operating range, the system becomes more prone to self-excited vibration.

Under a large initial disturbance, the initial displacement and velocity of the rotor deviate considerably from the equilibrium position. As shown in Figure 4, compared with the small-disturbance case, the rotor system enters the nonlinear response region more rapidly under a large disturbance. The vibration frequency increases, the instability process develops faster, and the post-bifurcation limit cycle exhibits a larger amplitude. This behavior indicates that the current-induced Hopf bifurcation is governed not only by the electromagnetic support parameters, but also by the magnitude of the initial disturbance.



(**a**) time history in the x direction (**b**) time history in the y direction

(**c**) phase trajectory in the x direction (**d**) phase trajectory in the y direction

(**e**) global bifurcation diagram in the x direction (**f**) global bifurcation diagram in the y direction

Figure 4. Bifurcation diagram of current i_0 under a large initial disturbance.

From the viewpoint of the dynamic mechanism, an increase in the current i_0 enhances the nonlinearity of the electromagnetic suspension force with respect to air gap variation, thereby changing the equivalent stiffness and equivalent damping of the system. When the current approaches the bifurcation boundary, the characteristic roots associated with the lateral vibration modes cross the imaginary axis, causing the equilibrium point to lose stability and giving rise to periodic vibration. A larger initial disturbance makes the system more likely to exceed the boundary of the local stability domain, which results in a faster instability process and a more pronounced limit cycle response.

3.2. Effect of Flow Rate q_0 on Hopf Bifurcation Behavior

The supply flow rate q_0 is a key operating parameter in the hydrostatic support system. Variations in flow rate affect the supporting chamber pressure, liquid film thickness, hydraulic resistance, and oil film damping, thereby changing the hydrostatic supporting force and the restoring capability of the system. Therefore, by taking the flow rate q_0 as the bifurcation parameter, the influence of the hydrostatic support subsystem on the Hopf bifurcation behavior of the rotor can be analyzed.

According to the Routh–Hurwitz criterion, the Hopf bifurcation boundary of the three-degree-of-freedom rotor system under the effect of the flow rate q_0 is obtained as $q_0 = 9.62 \times 10^{-5}$ m^3/s. When the supply flow rate approaches this critical value, the equilibrium state of the system loses stability, and a periodic response emerges near the equilibrium point.

Under a small initial disturbance, the flow rate is set to $q_0 = 2 \times 10^{-4}$ m^3/s for simulation. The time-history response in Figure 5 shows that the rotor remains in stable suspension in the x direction only during the first approximately 0.4 s. The vibration amplitude then increases rapidly and, after a transition lasting about 0.1 s, develops into self-excited vibration with a stable amplitude range of approximately $(-1.3 \times 10^{-7}, 1.3 \times 10^{-7})$ m. In the y direction, the rotor remains in stable suspension during 0–0.2 s. During 0.2–0.5 s, the vibration amplitude increases rapidly and reaches a maximum range of approximately $(-7.5 \times 10^{-7}, 7.5 \times 10^{-7})$ m. Subsequently, during 0.2–1.6 s, the vibration amplitude gradually decays and stabilizes within a range of approximately $(-2 \times 10^{-7}, 2 \times 10^{-7})$ m, forming a self-excited vibration.

The spatial phase trajectories show that, as the flow rate q_0 increases from the bifurcation boundary of 9.62×10^{-5} m^3/s to 1×10^{-3} m^3/s, the x-direction response consistently exhibits subcritical Hopf bifurcation. In the y direction, the system exhibits subcritical Hopf bifurcation when the flow rate is lower than 5×10^{-4} m^3/s, whereas supercritical Hopf bifurcation occurs when the flow rate exceeds 5×10^{-4} m^3/s. This indicates that variations in flow rate not only determine whether bifurcation occurs but also affect the type of bifurcation.

From the viewpoint of the physical mechanism, the flow rate q_0 directly affects the oil supply condition in the hydrostatic supporting chamber. At relatively low flow rates, the oil film load-carrying capacity and damping effect are insufficient. As a result, the rotor is less able to return to the equilibrium position after being disturbed, and the system is more prone to self-excited vibration. When the flow rate increases to a certain range, the hydrostatic supporting capacity is enhanced and the oil film damping increases, which improves the disturbance suppression capability of the system. Under this condition, the bifurcation behavior may transition from subcritical Hopf bifurcation to supercritical Hopf bifurcation.

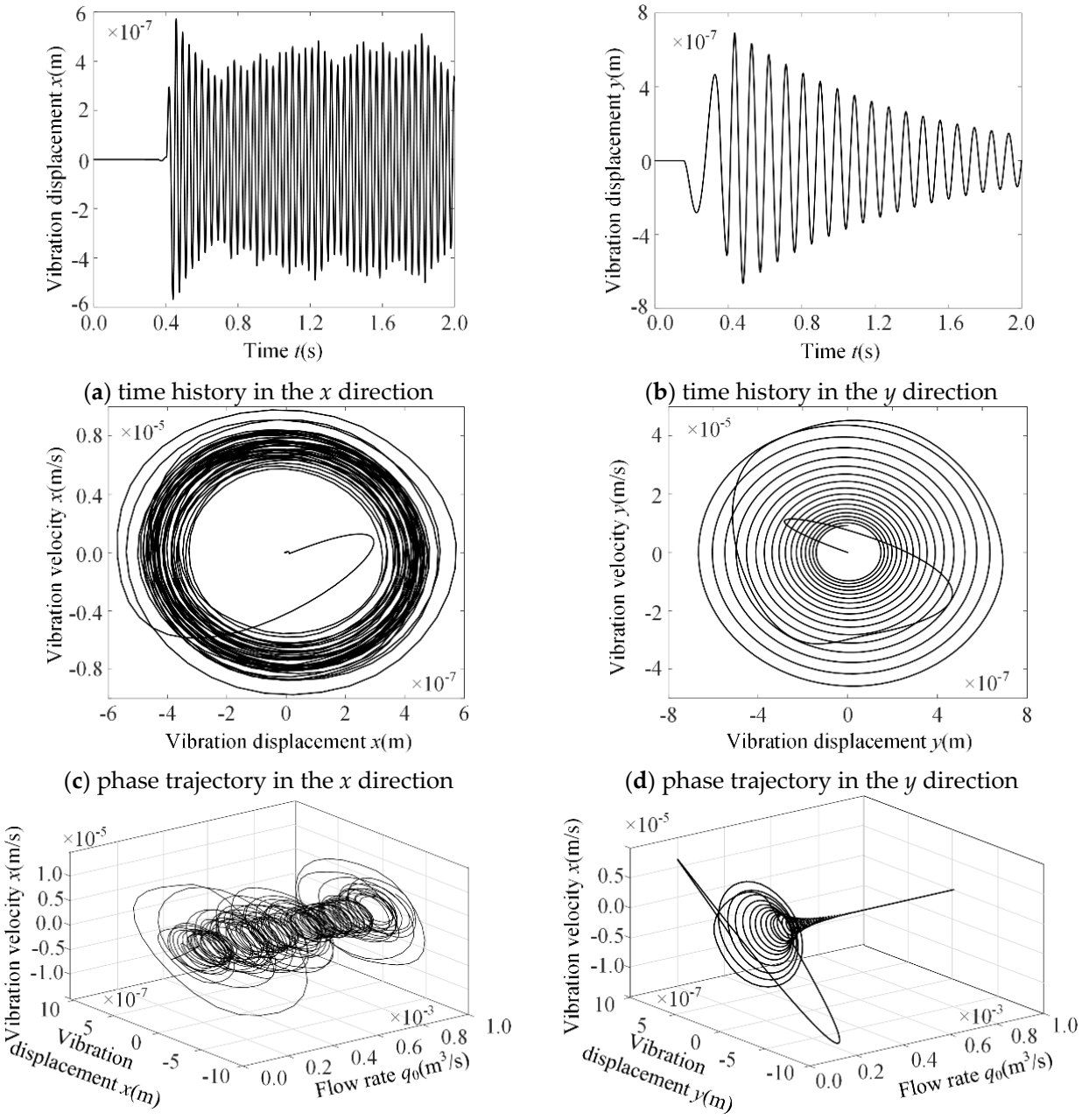
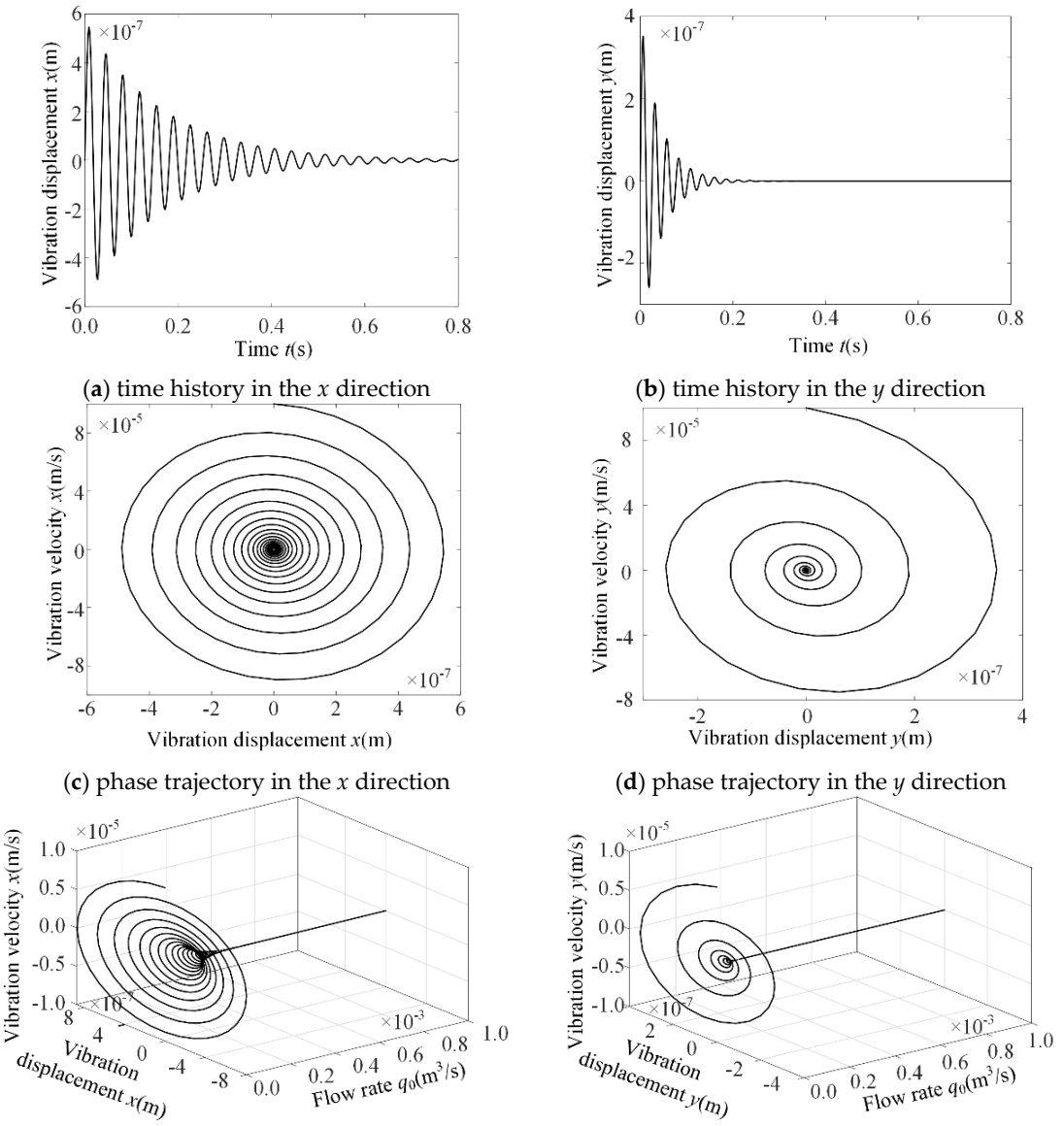


Figure 5. Bifurcation diagram of flow rate q_0 under a small initial disturbance.

Under a large initial disturbance, the initial state of the rotor is far from the equilibrium position. As shown in Figure 6, the rotor exhibits a strong disturbance recovery capability in both the x and y directions. The vibration amplitude gradually decreases, and the rotor eventually returns to stable suspension near the equilibrium position. Therefore, under this operating condition, the system exhibits supercritical Hopf bifurcation characteristics.

Compared with the small-disturbance case, the system under a large disturbance does not continuously develop a large amplitude limit cycle, but instead decays gradually toward the vicinity of the equilibrium position. This indicates that the influence of flow rate on system stability is related to the magnitude of the initial disturbance. When the restoring force and damping effect provided by the hydrostatic support are sufficient, the system may return to a stable suspension state even under a relatively large initial disturbance.



(**a**) time history in the x direction (**b**) time history in the y direction

(**c**) phase trajectory in the x direction (**d**) phase trajectory in the y direction

(**e**) global bifurcation diagram in the x direction (**f**) global bifurcation diagram in the y direction

Figure 6. Bifurcation diagram of flow rate q_0 under a large initial disturbance.

3.3. Two-Parameter Hopf Bifurcation Behavior with Respect to Current i_0 and Flow Rate q_0

The essential feature of a magnetic liquid double-suspension bearing is the combined action of electromagnetic suspension support and hydrostatic support. Varying only the current or the flow rate reflects the influence of a single supporting subsystem on rotor stability. In practical operation, however, the current i_0 and flow rate q_0 usually affect the dynamic characteristics of the system simultaneously. It is therefore necessary to further investigate the Hopf bifurcation behavior under their coupled effects.

3.3.1. Hopf Bifurcation Boundary with Respect to Current i_0 and Flow Rate q_0

Bifurcation diagrams can generally be generated using direct numerical integration, the Poincaré section method, the numerical continuation method, or the stability-criterion-based method. Taking the current i_0 and flow rate q_0 simultaneously as bifurcation parameters, the two-parameter Hopf bifurcation boundary is determined by substituting them into the characteristic equation of the system and applying the Routh–Hurwitz criterion. The stable and unstable regions in the current-flow-rate parameter plane can then be obtained.

In this process, the i_0-q_0 parameter plane is scanned over the prescribed ranges, while the other parameters are kept constant. For each parameter combination, the coefficients of the characteristic polynomial are calculated and substituted into the Routh–Hurwitz criterion. The parameter points satisfying the Hopf critical condition are regarded as boundary points. By plotting and connecting these critical points, the two-parameter Hopf bifurcation boundary shown in Figure 7 is obtained.

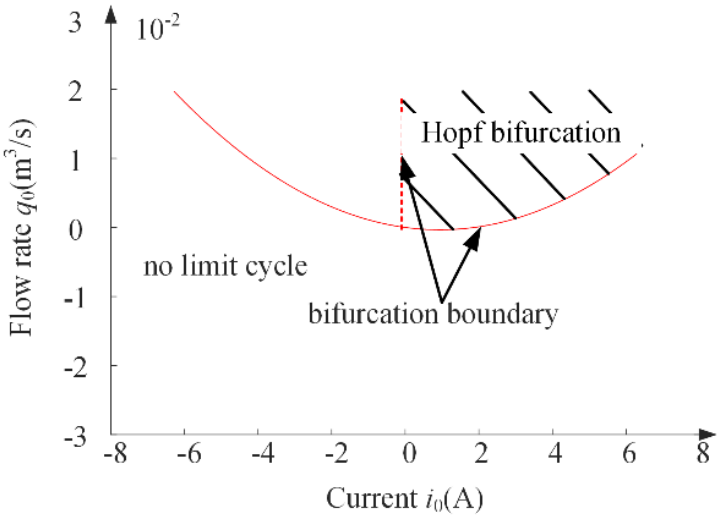


Figure 7. Hopf bifurcation boundary with two varying parameters.

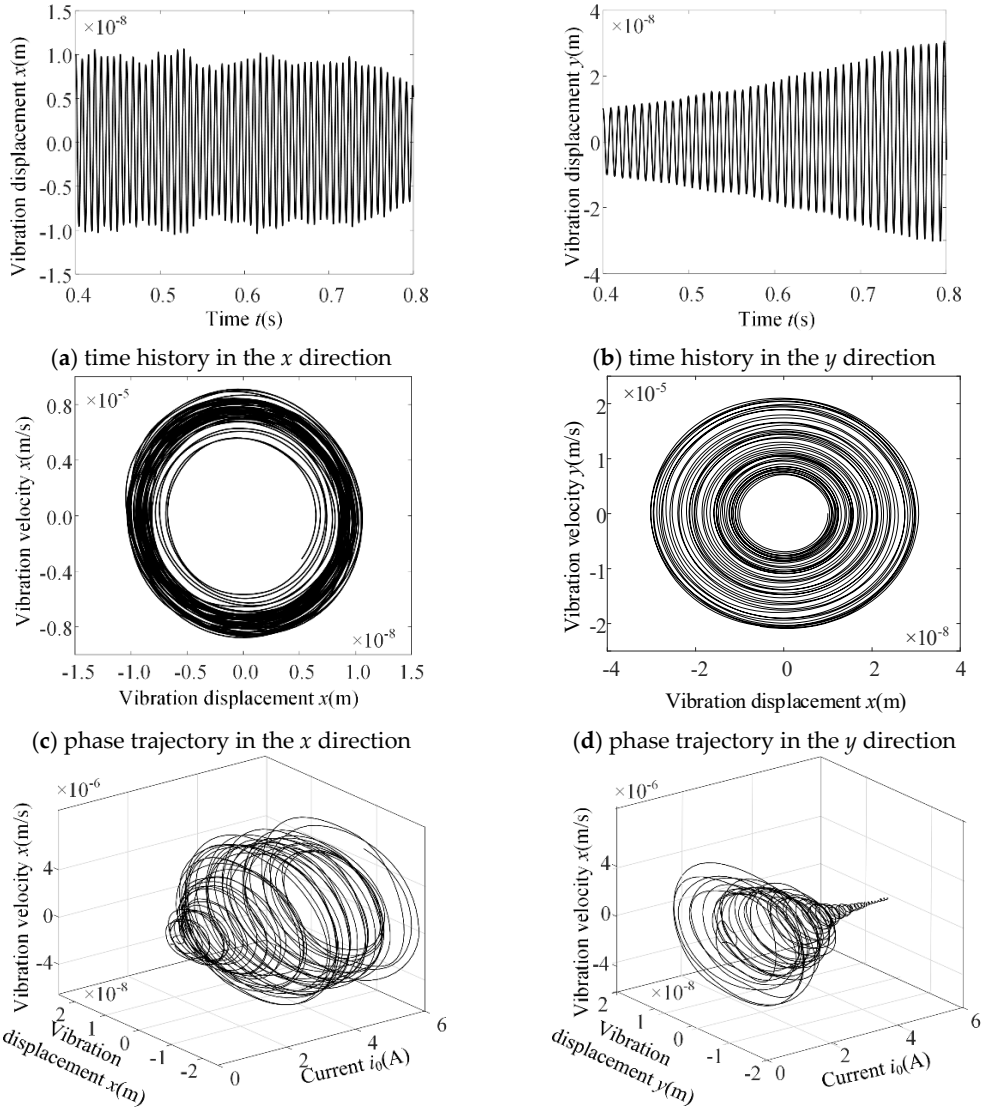
As shown in Figure 7, under the physical constraint that both the current and the flow rate are positive, the Hopf bifurcation boundary of the system in the two-parameter case is obtained within the ranges $i_0 \in (0, 6)$ A and $q_0 \in (0, 0.02)$ m^3/s. This boundary divides the parameter plane into a stable region and a Hopf bifurcation region. When the parameter combination is located in the stable region, the rotor maintains stable suspension. Once the combined current and flow rate cross the bifurcation boundary, the equilibrium point of the system loses stability, and periodic vibration is generated.

It should be noted that the Hopf bifurcation boundary under the combined effects of the two parameters is not a simple superposition of the single-parameter boundary for current and the single-parameter boundary for flow rate. Variations in current change the electromagnetic supporting stiffness, whereas variations in flow rate alter the hydrostatic supporting stiffness and oil film damping. Together, these effects determine the distribution of the characteristic roots of the system. Therefore, even if either parameter alone does not fully satisfy the instability condition, the system may still enter the bifurcation region when the combination of the two parameters is inappropriate.

3.3.2. Hopf Bifurcation Response Under Two-Parameter Coupling with Current as the Variable

Based on the two-parameter bifurcation boundary, the current i_0 is first selected as the varying parameter, while the flow rate is fixed at $q_0 = 0.04$ m^3/s. The system responses under small and large initial disturbances are then analyzed separately.

As shown in Figure 8, under a small initial disturbance, the rotor exhibits self-excited vibration in both the x and y directions. The vibration amplitude is approximately $(-1 \times 10^{-8}, 1 \times 10^{-8})$ m in the x direction and approximately $(-3 \times 10^{-8}, 3 \times 10^{-8})$ m in the y direction. The phase trajectories form closed orbits, indicating that Hopf bifurcation occurs under the small-disturbance condition.



(**a**) time history in the x direction (**b**) time history in the y direction

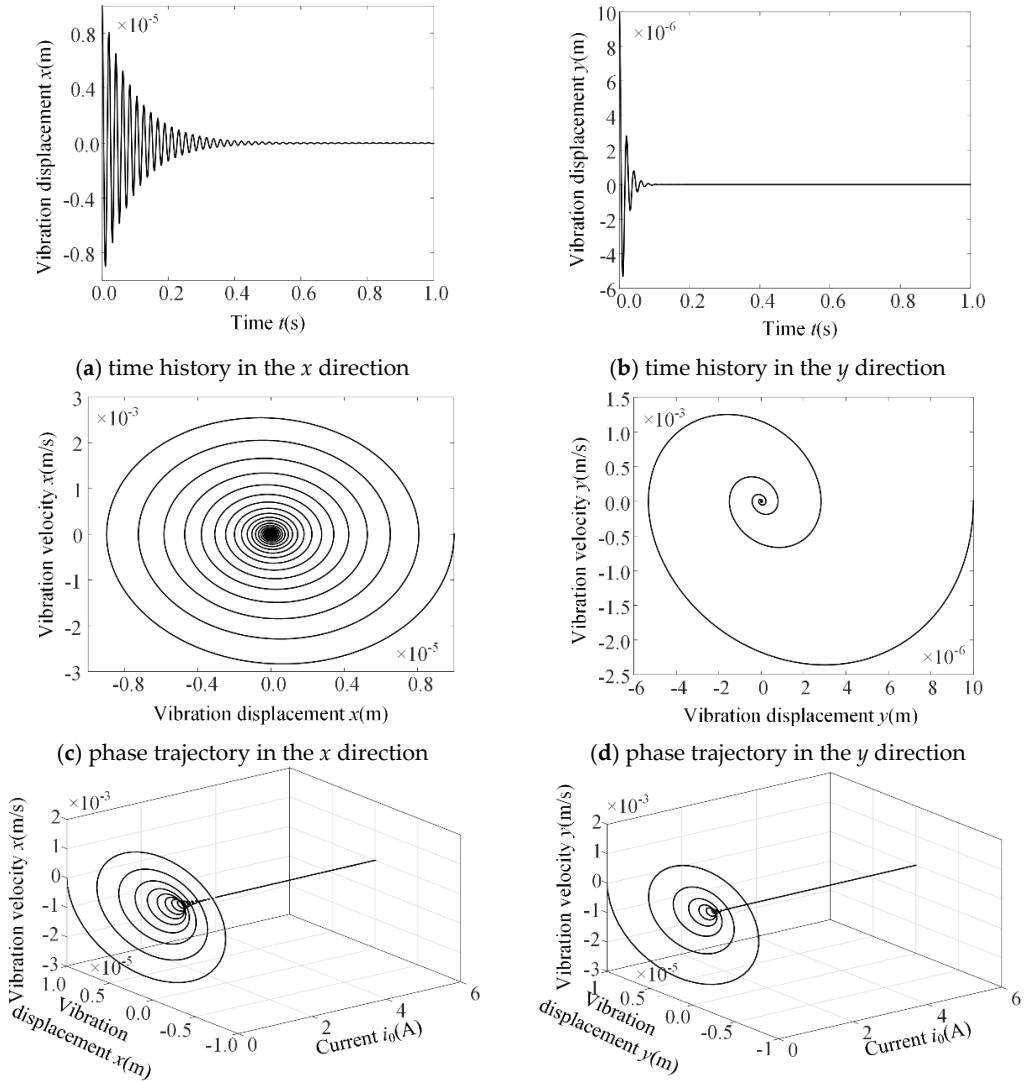
(**c**) phase trajectory in the x direction (**d**) phase trajectory in the y direction

(**e**) global bifurcation diagram in the x direction (**f**) global bifurcation diagram in the y direction

Figure 8. Bifurcation diagram of the two-parameter system with current as the variable under a small initial disturbance.

The spatial phase trajectories show that, when the current i_0 varies within the range of (0, 6) A, the x-direction response consistently exhibits subcritical Hopf bifurcation. At approximately i_0 = 3 A, the x-direction amplitude reaches its peak value of about 2×10^{-8} m. In contrast, the y-direction amplitude gradually decreases as the current varies and eventually approaches the vicinity of the equilibrium position. This indicates that, under the specified flow-rate condition, current variation is more likely to induce a limit cycle response in the x direction, whereas the y-direction response shows a tendency to transition from subcritical Hopf bifurcation to supercritical Hopf bifurcation.

As shown in Figure 9, under a large initial disturbance, the vibration amplitudes of the rotor in both the x and y directions decrease gradually with time, and the rotor eventually returns to stable suspension near the equilibrium position. This result indicates that, under this parameter combination, the large disturbance leads to a more intense initial response, but the system can ultimately resist the external disturbance and recover its stability. The response, therefore, exhibits the characteristics of supercritical Hopf bifurcation.



(**a**) time history in the x direction

(**b**) time history in the y direction

(**c**) phase trajectory in the x direction

(**d**) phase trajectory in the y direction

(**e**) global bifurcation diagram in the x direction

(**f**) global bifurcation diagram in the y direction

Figure 9. Bifurcation diagram of the two-parameter system with current as the variable under a large initial disturbance.

A comparison between Figures 8 and 9 indicates that the initial disturbance amplitude affects the post-bifurcation response pattern of the system. Under a small disturbance, the system is more likely to develop a stable limit cycle. Under a large disturbance, however, the system may cross the attraction domain of the local limit cycle and return to the vicinity of the equilibrium position under the combined effects of supporting restoring force and damping. Therefore, under current-flow-rate coupling, the bifurcation type of the system may transition from subcritical Hopf bifurcation to supercritical Hopf bifurcation.

3.3.3. Hopf Bifurcation Response Under Two-Parameter Coupling with Flow Rate as the Variable

The flow rate q_0 is further selected as the varying parameter, while the current is fixed at $i_0 = 7$ A. The response of the rotor system to variations in flow rate under two-parameter coupling is then analyzed.

As shown in Figure 10, under a small initial disturbance, the vibration amplitude of the rotor in the x direction gradually decreases but still develops into self-excited vibration with a finite amplitude. The stable amplitude is approximately 2×10^{-6} m. In contrast, the y-direction amplitude decays gradually, and the rotor eventually returns to the vicinity

of the equilibrium position. These responses indicate that under this operating condition, the x-direction motion remains periodic, whereas the y-direction motion exhibits greater stability recovery capability.

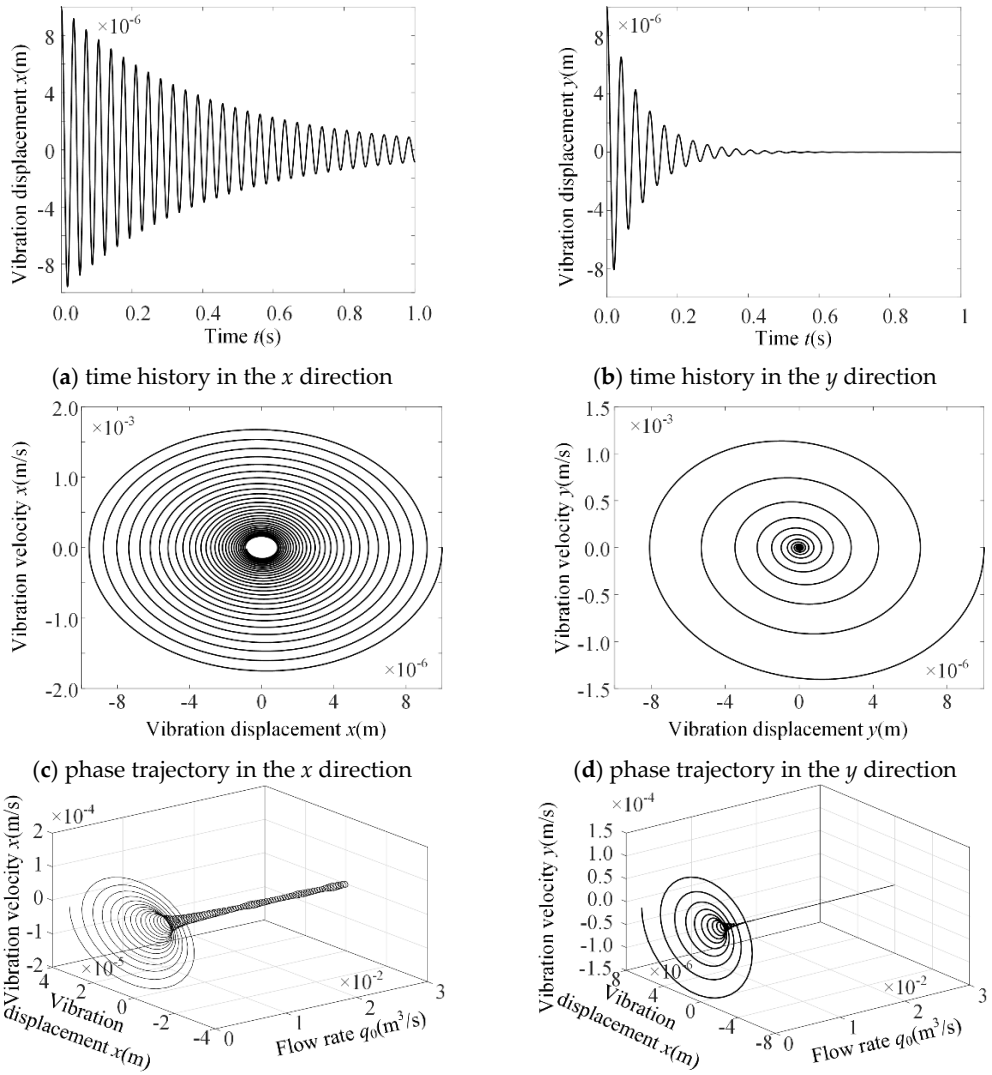
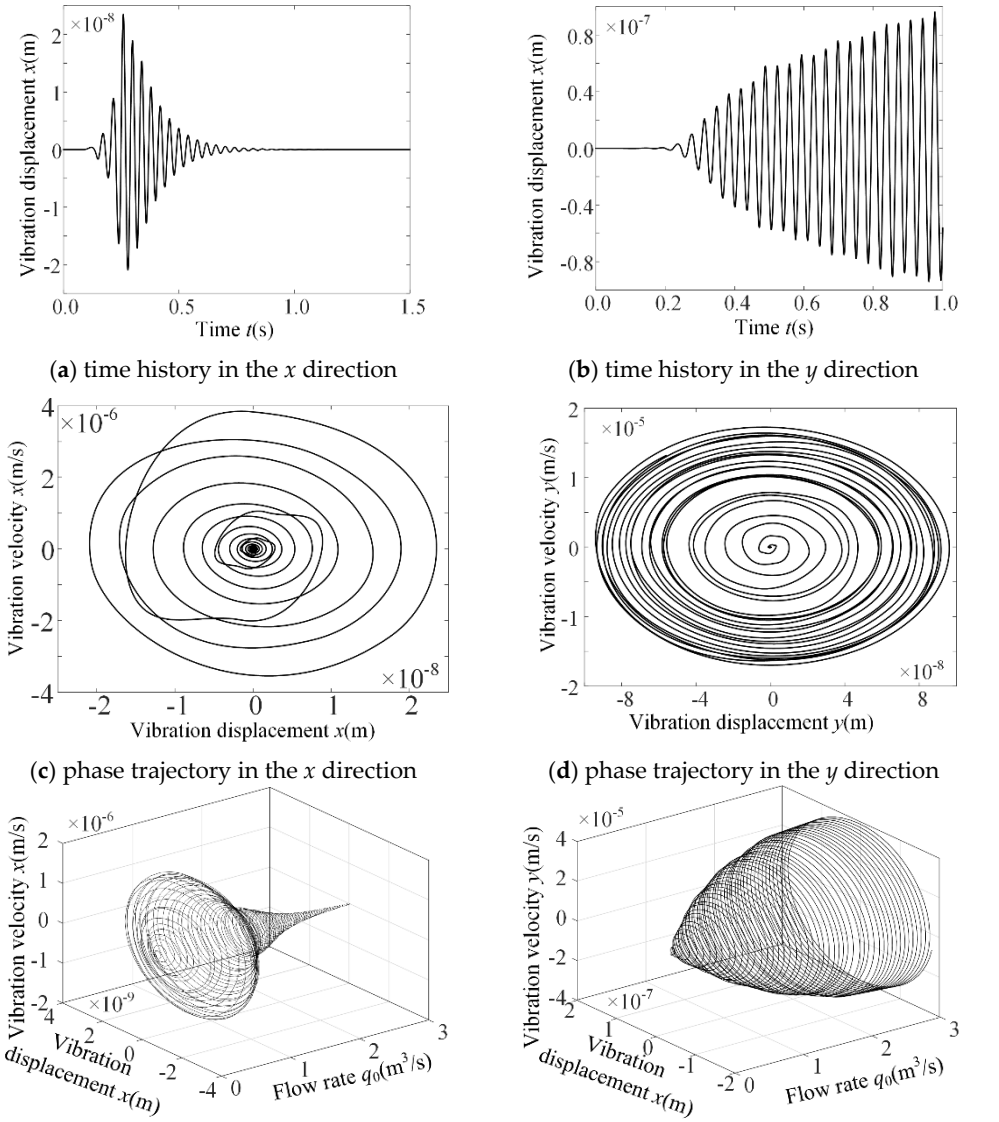


Figure 10. Bifurcation diagram of the two-parameter system with flow rate as the variable under a small initial disturbance.

The flow rate scanning results further show that, as q_0 is varied, the x-direction response undergoes subcritical Hopf bifurcation. Its amplitude first decreases and then reaches a stable level of approximately 2×10^{-6} m. In the y direction, the system exhibits subcritical Hopf bifurcation when $q_0 \in (0, 5) \times 10^{-3}$ m^3/s, whereas it exhibits supercritical Hopf bifurcation when $q_0 \in (5, 30) \times 10^{-3}$ m^3/s. This result suggests that variations in flow rate have a more pronounced regulating effect on the stability of the y-direction response.

As shown in Figure 11, under a large initial disturbance, the rotor amplitude in the x direction first increases and then gradually decays, eventually approaching a stable state. In contrast, the y-direction amplitude gradually increases and then remains within a finite range, forming a stable periodic response with a stable amplitude of approximately 2×10^{-7} m. This indicates that, under two-parameter coupling with flow rate as the varying parameter, a large initial disturbance alters the amplitude evolution process of the system.

The x-direction response exhibits stronger decay and recovery capability, whereas the y-direction response is more likely to develop into a stable limit cycle.



(**a**) time history in the x direction (**b**) time history in the y direction

(**c**) phase trajectory in the x direction (**d**) phase trajectory in the y direction

(**e**) global bifurcation diagram in the x direction (**f**) global bifurcation diagram in the y direction

Figure 11. Bifurcation diagram of the two-parameter system with flow rate as the variable under a large initial disturbance.

From the mechanistic perspective, variations in flow rate directly affect the load-carrying capacity and damping characteristics of the hydrostatic oil film. The y-direction response is also governed by the balance between gravity and supporting force, making it more sensitive to flow rate variation. When the flow rate is in a relatively low range, the oil film damping is insufficient, and the system is more prone to subcritical Hopf bifurcation. As the flow rate increases, the hydrostatic support becomes stronger and the recovery capability of the system improves, so that the bifurcation type gradually tends to shift toward supercritical Hopf bifurcation.

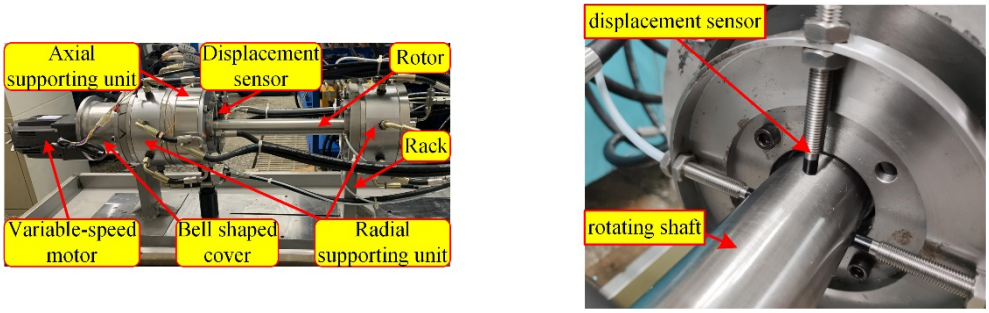
4. Experimental Validation

To validate the effectiveness of the three-degree-of-freedom dynamic model of the magnetic liquid double-suspension bearing rotor system and the corresponding Hopf bifurcation analysis results, a magnetic liquid double-suspension bearing test system is

constructed. The displacement responses of the rotor are acquired under stable suspension and parameter disturbance conditions. By comparing the frequency spectra, time histories, and phase trajectories obtained from numerical simulations and experiments, the predictive capability of the three-degree-of-freedom dynamic model for rotor vibration characteristics and bifurcation response trends is evaluated.

4.1. Experimental System and Measurement Method

The magnetic liquid double-suspension bearing test system (self-developed, Yanshan University, Qinhuangdao, China) consists mainly of three parts: the bearing body, the oil-supply hydraulic pump station, and the electronic control system. The bearing body provides combined electromagnetic and hydrostatic support for the rotor. The oil-supply hydraulic pump station supplies a stable flow rate to the hydrostatic supporting chambers, while the electronic control system regulates the coil current and control parameters to control the rotor suspension position. The overall structure and main components of the test rig are shown in Figures 12–14.



(**a**) The overall structure of the bearing body (**b**) Rotating shaft and displacement sensor

Figure 12. Magnetic liquid double-suspension bearing body.

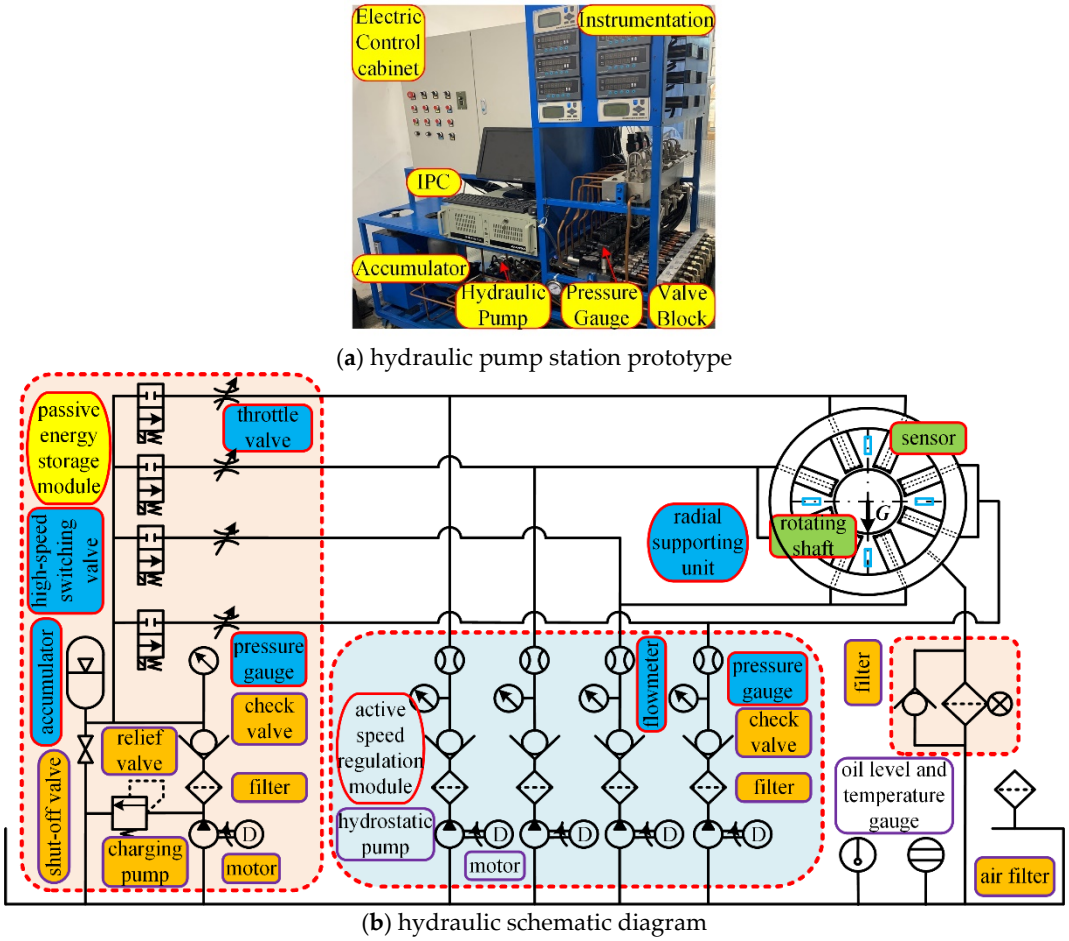
As shown in Figure 12, the bearing body mainly consists of a variable-speed motor, a rotating shaft, a bell-shaped housing, radial and axial bearings, and displacement sensors. To monitor rotor displacement in real time, displacement sensors are installed at the right end of the radial bearing. The acquired displacement signals are transmitted to the industrial computer through a data acquisition card for rotor suspension monitoring and data processing.

As shown in Figure 13, the hydraulic pump station mainly includes an electro-hydraulic pump, a control valve block, an accumulator, a pressure gauge, a flowmeter, and a filter, and is used to provide a stable oil supply for the hydrostatic supporting units. The electronic control system consists of an electrical control cabinet, a power amplifier, a sensor signal acquisition module, and a magnetic liquid-coupled bearing acquisition and control program, which are used to achieve coordinated control of the electromagnetic support and hydrostatic support.

During the experiment, the electronic control system and hydraulic pump station are started first. The initial rotor offset is adjusted in the acquisition and control program so that, under the stationary condition, the rotor is located near the relative center of the radial and axial bearings. The coupled electromagnetic and hydrostatic control mode is then activated. The voltage offset and PID parameters are adjusted, and the variable-speed motor is started to enable stable rotational suspension of the rotor near the center position.

After the system reaches a stable operating state, the displacement data transmitted from the displacement sensors to the data-acquisition card are extracted. The rotor frequency spectrum is then obtained and compared with the numerical simulation results under the same operating conditions. Subsequently, the current i_0 and flow rate q_0 are adjusted to match the operating conditions used in the three-degree-of-freedom

two-parameter simulations. The rotor displacement data are collected to generate phase trajectories and time-history curves, which are used to evaluate the reliability of the simulation results. In the Hopf bifurcation experiments for the three-degree-of-freedom system, the displacement data are used to construct frequency spectra, phase trajectories, and time histories for comparison with the numerical simulations.



(**a**) hydraulic pump station prototype

(**b**) hydraulic schematic diagram

Figure 13. Oil supply hydraulic pump station of the magnetic liquid double-suspension bearing.

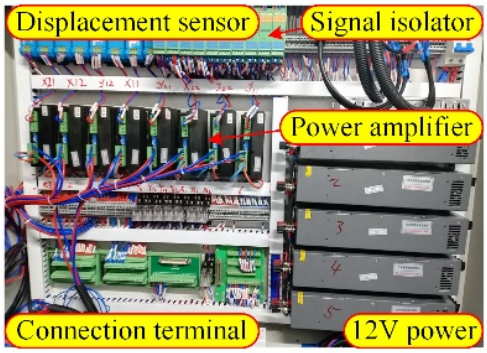


Figure 14. Electronic control system of the magnetic liquid double-suspension bearing.

4.2. Frequency Spectrum Response Validation

To validate the ability of the three-degree-of-freedom dynamic model to predict the dominant frequency components of the rotor, frequency spectrum analysis is performed on the rotor displacement signals under stable suspension conditions, and the results are compared with those obtained from numerical simulations.

As shown in Figure 15, within the dimensionless frequency ratio range of 0–5, both the numerical simulation and experimental results exhibit frequency components at ω–9ω. This indicates that the established three-degree-of-freedom dynamic model can capture the dominant frequency response characteristics of the magnetic liquid double-suspension bearing rotor system. In particular, good agreement between the simulation and experimental results is observed near the 2ω component, where the response amplitude is relatively large. The amplitude distributions at the other frequency components also follow similar trends.

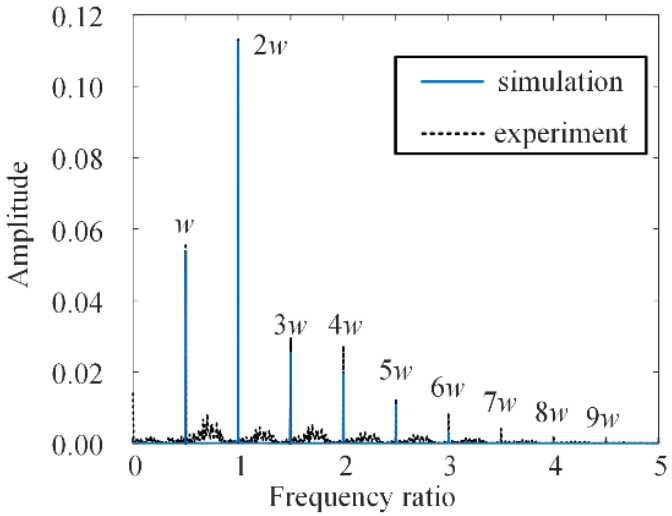


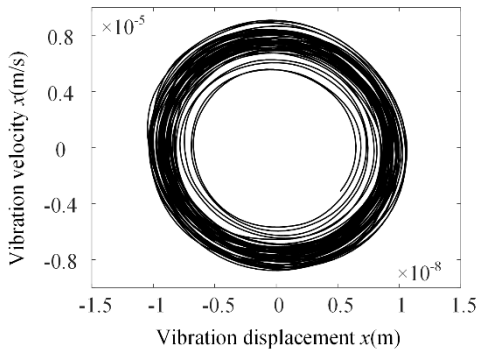
Figure 15. Frequency spectra obtained from numerical simulation and experiment.

The frequency spectrum results show that the rotor response is not limited to a single fundamental vibration but contains multiple harmonic components. This indicates that the magnetic liquid double-suspension bearing rotor system exhibits pronounced nonlinear response characteristics under the combined action of electromagnetic force, hydrostatic supporting force, and rotor unbalance force. The agreement between the simulation and experimental results at the dominant frequency components demonstrates that the three-degree-of-freedom model can describe the principal frequency and harmonic responses of the system with reasonable accuracy, thereby providing experimental support for the subsequent analysis of Hopf bifurcation responses.

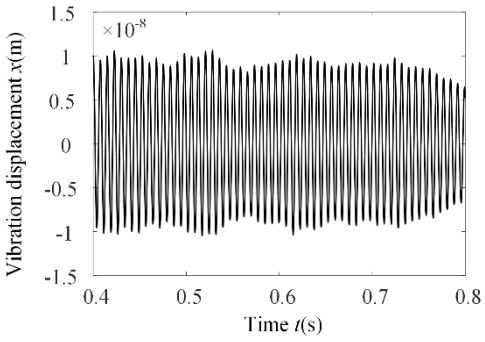
4.3. Validation Based on Time Histories and Phase Trajectories

On the basis of the frequency spectrum validation, the time histories and phase trajectories of the rotor in the x and y directions are further compared to evaluate the ability of the three-degree-of-freedom model to describe post-bifurcation periodic responses and limit cycle characteristics.

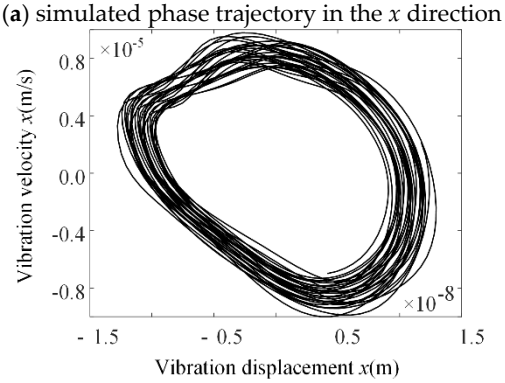
As shown in Figure 16, the rotor displacement responses obtained from both simulation and experiment exhibit periodic vibration characteristics. In the x direction, both the simulated and experimental phase trajectories form closed orbits, indicating that the system develops a stable periodic response under this operating condition. The corresponding time-history curves also show a relatively stable periodic vibration pattern. In the y direction, the simulation and experimental results likewise exhibit periodic response characteristics, demonstrating that limit cycle motion associated with Hopf bifurcation is formed in both radial directions. Figure 16 presents the simulated and experimental phase trajectories and time histories in the x direction, along with the corresponding simulated and experimental results in the y direction.



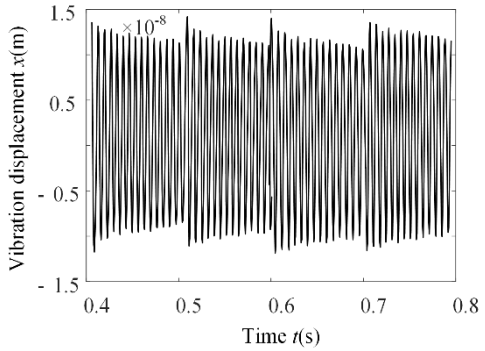
(**a**) simulated phase trajectory in the *x* direction



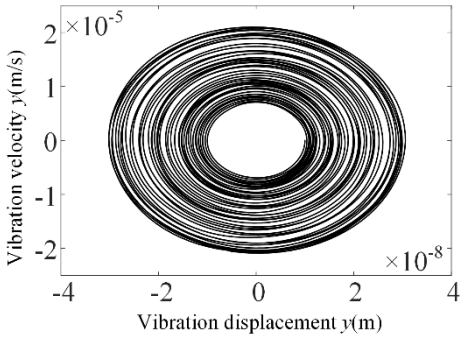
(**b**) simulated time history in the *x* direction



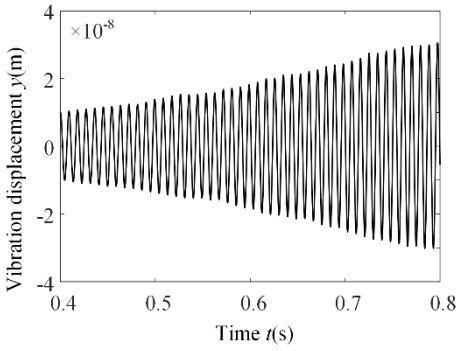
(**c**) experimental phase trajectory in the *x* direction



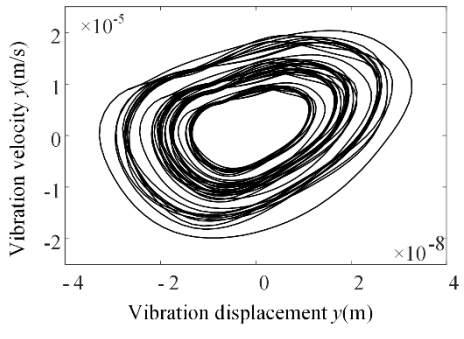
(**d**) experimental time history in the *x* direction



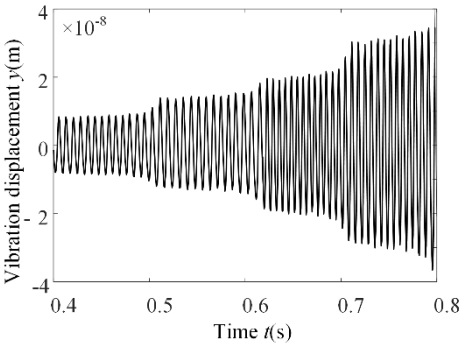
(**e**) simulated phase trajectory in the *y* direction



(**f**) simulated time history in the *y* direction



(**g**) experimental phase trajectory in the *y* direction



(**h**) experimental time history in the *y* direction

Figure 16. Comparison of simulated and experimental time histories and phase trajectories under two-parameter variation.

The comparison in Figure 16 shows that the simulation and experimental curves are in good agreement in terms of vibration trend, phase-trajectory pattern, and amplitude order. The closed-phase trajectories indicate that the rotor develops stable periodic motion after bifurcation. The time-history curves exhibit sustained periodic variations, suggesting that the system does not diverge but enters a finite-amplitude self-excited vibration state. This

behavior is consistent with the Hopf bifurcation response characteristics obtained from the Routh–Hurwitz criterion and numerical simulations discussed above.

To further strengthen the comparison between simulation and experiment, representative quantitative information is added based on the existing results. The dominant frequency component of both the numerical simulation and experiment appears near 2ω, showing consistency in the main frequency response. In addition, the simulated and experimental response amplitudes in both radial directions are within the same order of magnitude. For example, the x-direction response amplitude obtained from the simulation is approximately $(-1.0 \times 10^{-8}, 1.0 \times 10^{-8})$ m, while the experimental result is approximately $(-1.2 \times 10^{-8}, 1.2 \times 10^{-8})$ m. The y-direction amplitudes obtained from simulation and experiment are both approximately within $(-3.0 \times 10^{-8}, 3.0 \times 10^{-8})$ m. These results indicate that the proposed model can reasonably capture the dominant frequency and representative amplitude characteristics of the rotor system.

Nevertheless, certain discrepancies remain between the simulated and experimental curves. These discrepancies can be attributed mainly to the following factors. First, local linearization and approximate treatments are adopted in the theoretical model, whereas the nonlinearities associated with electromagnetic force, oil film force, and structural errors are more complex in the actual system. Second, machining and assembly errors in the bearing body may cause a slight deviation between the actual motion center of the rotor and the theoretical equilibrium point. Third, fluctuations in the oil supply flow rate and pressure of the hydraulic system may lead to transient variations in the hydrostatic supporting force. In addition, the displacement sensors and data acquisition system may introduce measurement noise. The experimental summary also indicates that the overall operating trends obtained from simulation and experiment are basically consistent, although certain deviations remain in rotor vibration velocity, amplitude, and frequency owing to model approximations and manufacturing errors of the test rig.

Taken together, the frequency spectra, time histories, and phase trajectories indicate that the three-degree-of-freedom dynamic model can predict the dominant frequency responses and post-bifurcation periodic motion characteristics of the magnetic liquid double-suspension bearing rotor with reasonable accuracy. The experimental results validate the rationality of the theoretical model and numerical simulations from both the frequency-domain and time-domain perspectives. These findings demonstrate that the established model is suitable for analyzing the Hopf bifurcation behavior of the rotor under the coupled effects of current and flow rate.

5. Conclusions

This study investigated a three-degree-of-freedom rotor system supported by a magnetic liquid double-suspension bearing. A nonlinear dynamic model incorporating electromagnetic suspension force, hydrostatic supporting force, rotor unbalance force, and liquid film resistance was established. Based on the Routh–Hurwitz criterion, the Hopf bifurcation behavior of the system was analyzed under the effects of current i_0, supply flow rate q_0, and their coupling. Numerical simulations and experimental validation led to the following conclusions:

(1) The established three-degree-of-freedom rotor dynamic model can describe the coupled nonlinear characteristics of electromagnetic support and hydrostatic support in the magnetic liquid double-suspension bearing. Based on equilibrium point linearization and the Routh–Hurwitz criterion, the Hopf bifurcation boundary of the rotor system under current and flow rate parameters can be obtained. This provides a theoretical basis for analyzing the transition of the rotor from stable suspension to periodic vibration.

(2) The current i_0 has a substantial influence on the stability of the rotor system. Under the parameter conditions considered in this study, the Hopf bifurcation boundary with current as the single parameter is i_0 = 0.61 A. When the current exceeds this critical value, the nonlinearity of the electromagnetic suspension force with respect to air gap variation is enhanced, and the equivalent stiffness and damping characteristics of the system change accordingly. As a result, periodic vibration may occur in both the x and y directions. A larger initial disturbance amplitude makes the system more likely to enter the nonlinear response region rapidly.

(3) The supply flow rate q_0 mainly affects rotor stability by changing the load-carrying capacity and damping characteristics of the hydrostatic oil film. Under the parameter conditions considered in this study, the Hopf bifurcation boundary with flow rate as the single parameter is $q_0 = 9.62 \times 10^{-5}$ m^3/s. When the flow rate approaches the critical value, the equilibrium state of the system loses stability and a periodic response is generated. Compared with the effect of current, the influence of flow rate on the stability in the y direction is more pronounced, because the y direction is also affected by the balance between gravity and hydrostatic supporting force.

(4) Under the coupled effects of current and flow rate, system stability is no longer determined by a single parameter, but by the combined effects of electromagnetic supporting stiffness, hydrostatic supporting stiffness, and oil film damping. The two-parameter Hopf bifurcation boundary indicates that appropriate matching between current and flow rate can enlarge the stable suspension region of the system. When the two parameters are not properly matched, the system may still enter the Hopf bifurcation region and generate self-excited vibration, even if neither parameter individually exceeds the stable range.

(5) The initial disturbance amplitude affects the post-bifurcation amplitude evolution and limit cycle response. Under small initial disturbances, the rotor is more likely to develop finite amplitude periodic vibration near the bifurcation boundary. Under large initial disturbances, the system may exhibit amplitude decay, stable recovery, or sustained periodic response. This indicates that the stable operation of the magnetic liquid double-suspension bearing depends not only on the matching of current and flow rate, but also on the intensity of external disturbances.

(6) The experimental results agree well with the numerical simulation results in terms of frequency spectrum distribution, time-history evolution, and phase-trajectory pattern. The dominant frequency components in the rotor displacement spectrum can be predicted by the model with reasonable accuracy. Comparisons of the phase trajectories and time histories further indicate that the model can capture the periodic response characteristics generated after the Hopf bifurcation. Therefore, the established three-degree-of-freedom dynamic model and bifurcation analysis method can provide a useful reference for operating parameter design and stability regulation of magnetic liquid double-suspension bearings.

Author Contributions: Conceptualization, X.W. and J.Z.; methodology, X.W., X.Z. and H.Z.; software, X.W.; validation, X.W., X.Z., H.Z. and J.Z.; formal analysis, X.W. and H.Z.; investigation, X.W., X.Z. and H.Z.; resources, J.Z.; data curation, X.W. and H.Z.; writing—original draft preparation, X.W.; writing—review and editing, X.Z., H.Z. and J.Z.; visualization, X.W. and H.Z.; supervision, J.Z.; project administration, J.Z.; funding acquisition, J.Z. All authors have read and agreed to the published version of the manuscript.

Funding: The research leading to these results received funding from [Hebei Province Central Guided Local Science and Technology Development Fund] under Grant Agreement No [236Z1901G].

Data Availability Statement: The raw data supporting the conclusions of this article will be made available by the authors on request.

Conflicts of Interest: The authors declare no conflicts of interest.

References

1. Yu, X.; Gao, W.; Feng, Y.; Shi, G.; Li, S.; Chen, M.; Zhang, R.; Wang, J.; Jia, W.; Jiao, J.; et al. Research progress of hydrostatic bearing and hydrostatic-hydrodynamic hybrid bearing in high-end computer numerical control machine equipment. *Int. J. Precis. Eng. Manuf.* **2023**, *24*, 1053–1081. [CrossRef]
2. Michalec, M.; Svoboda, P.; Křupka, I.; Hartl, M. A review of the design and optimization of large-scale hydrostatic bearing systems. *Eng. Sci. Technol. Int. J.* **2021**, *24*, 936–958. [CrossRef]
3. Srinivas, R.S.; Tiwari, R.; Kannababu, C. Application of active magnetic bearings in flexible rotordynamic systems–A state-of-the-art review. *Mech. Syst. Signal Process.* **2018**, *106*, 537–572.
4. Zhao, J.; Zhang, H.; Qin, B.; Wang, Y.; Wu, X.; Han, F.; Du, G. Influence of Controller's Parameters on Static Bifurcation of Magnetic-Liquid Double Suspension Bearing. *Energies* **2021**, *14*, 8241. [CrossRef]
5. Zhao, J.; Yan, W.; Han, F.; Ma, X.; Xing, L.; Du, G. Supporting performance of magnetic-liquid double suspension bearing under wear of magnetic poles. *Desalination Water Treat.* **2022**, *253*, 270–284. [CrossRef]
6. Lee, G.-Y.; Park, M.; Ahn, K. Nonlinear vibration analysis of rotor systems with hydrodynamic journal bearings using harmonic balance method. *Int. J. Non-Linear Mech.* **2025**, *170*, 104992.
7. Lin, R.; Hou, L.; Zhong, S.; Chen, Y. Nonlinear vibration and stability analysis of a dual-disk rotor-bearing system under multiple frequency excitations. *Nonlinear Dyn.* **2024**, *112*, 12815–12846.
8. Ma, W.; Liu, F.; Lu, S.; Song, X.; Huang, S.; Zhu, Y.; Jiang, X. Nonlinear dynamics and motion bifurcations of 12-pole variable stiffness rotor active magnetic bearings system under complex resonance. *Int. J. Non-Linear Mech.* **2025**, *169*, 104958.
9. Zhang, L. Hopf bifurcation and vibration control for a thrust magnetic bearing with variable load mass. *Sensors* **2018**, *18*, 2212. [CrossRef] [PubMed]
10. Ji, J.; Hansen, C.H. Hopf bifurcation of a magnetic bearing system with time delay. *J. Vib. Acoust.* **2005**, *127*, 362–369.
11. Zhang, L.; Huang, L.; Zhang, Z. Stability and Hopf bifurcation of the maglev system with delayed position and speed feedback control. *Nonlinear Dyn.* **2009**, *57*, 197–207.
12. Wang, C.; Liu, C.; Cao, S.; Sun, L. Nonlinear vibration control of magnetic bearing system considering positive and negative stiffness. *J. Vib. Control* **2025**, *31*, 796–806.
13. Yao, H.; Inayat-Hussain, J.I. Nonlinear dynamics of a geared rotor system supported by active magnetic bearings. *J. Mech. Sci. Technol.* **2025**, *39*, 6479–6485. [CrossRef]
14. Kandil, A. Modeling and Control of Rotor Oscillations in Active Magnetic Bearings Using a Generalized Pole-Pair Approach. *J. Nonlinear Math. Phys.* **2026**, *33*, 52. [CrossRef]
15. Shen, G.; Xiao, Z.; Zhang, W.; Zheng, T. Nonlinear behavior analysis of a rotor supported on fluid-film bearings. *J. Vib. Acoust.* **2006**, *128*, 35–40.
16. Wang, J.; Khonsari, M. Prediction of the stability envelope of rotor-bearing system. *J. Vib. Acoust.* **2006**, *128*, 197.
17. Zhang, H.; Cheng, M.; Zhou, X.; Feng, L.; Feng, K. Investigations on the nonlinear dynamic characteristics of a rotor supported by hybrid foil magnetic bearings. *Nonlinear Dyn.* **2023**, *111*, 14879–14899. [CrossRef]
18. Zhang, X.; Wang, X.; Yang, J.; Zhang, Z.; Bai, K.; Chen, J.; Wang, Y.; Zhao, J. Study on chaotic dynamic behavior of magnetic liquid double-suspension bearings under rub-impact faults. *Proc. Inst. Mech. Eng. Part K J. Multi-Body Dyn.* **2025**, *239*, 293–306.
19. Ebrahimi, R.; Ghayour, M.; Khanlo, H.M. Nonlinear dynamic analysis and experimental verification of a magnetically supported flexible rotor system with auxiliary bearings. *Mech. Mach. Theory* **2018**, *121*, 545–562. [CrossRef]

Disclaimer/Publisher's Note: The statements, opinions and data contained in all publications are solely those of the individual author(s) and contributor(s) and not of MDPI and/or the editor(s). MDPI and/or the editor(s) disclaim responsibility for any injury to people or property resulting from any ideas, methods, instructions or products referred to in the content.